Three-Station Interferometry and Tomography Using Coda and Direct Waves

Shane Zhang[1], **Lili Feng**[1], **Michael H. Ritzwoller**[1]

[1] Center for Imaging the Earth's Interior, Department of Physics, University of Colorado Boulder, Boulder, CO 80309, USA.

Summary

Traditional two-station ambient noise interferometry estimates the Green's function between a pair of synchronously deployed seismic stations. Three-station interferometry considers records observed three stations at a time, where two of the stations are considered receiver-stations and the third is a source-station. Cross-correlations between records at the source-station with each of the receiver-stations are correlated or convolved again to estimate the Green's function between the receiver-stations, which may be deployed asynchronously. We use data from the EarthScope USArray in the western US to compare Rayleigh wave dispersion obtained from two-station and three-station interferometry. Three three-station interferometric methods are distinguished by the data segment utilized (coda-wave or direct-wave) and whether the source-stations are constrained to lie in stationary phase zones approximately inline with the receiver-stations. The primary finding is that the three-station direct wave methods perform considerably better than the three-station coda-wave method and two-station ambient noise interferometry, in terms of signal-to-noise ratio, bandwidth, and the number of measurements obtained, but possess small biases relative to two-station interferometry. We present a ray-theoretic correction method that largely removes the bias below 50 s period and reduces it at longer periods. Three-station direct-wave interferometry provides substantial value for imaging the crust and uppermost mantle, and its ability to bridge asynchronously deployed stations may impact the design of seismic networks in the future.

Key words: Seismic noise; Seismic interferometry; Seismic tomography; Surface waves and free oscillations; Coda waves.

Corresponding author: Shane Zhang, shzh3924@colorado.edu

1 Introduction

Inter-station seismic interferometry is designed to extract an estimate of the Green's function between pairs of seismic stations or receivers. Generally speaking, there are two established methods to perform this task, which we will call "*two-station interferometry*" and "*three-station interferometry*". In this paper, we attempt to clarify and illuminate three-station interferometry, discuss and characterize important variants of the method, and compare the characteristics amongst the variants and to two-station interferometry using data from the EarthScope Transportable Array (TA) in the US.

Two-station interferometry is the traditional method of "*ambient noise interferometry*" or "*ambient noise correlation*". It is the more commonly applied method and is based on a single cross-correlation between ambient noise recorded at two stations. The cross-correlation can be converted to an estimate of the Green's function of the medium if the time series is long enough (e.g., Shapiro & Campillo, 2004). In this case, one of the stations acts as a virtual source of the seismic energy and the other as the receiver. When many pairs of stations are considered, it is the basis for *ambient noise tomography* of surface waves, and many applications of this method have emerged since Shapiro et al. (2005); Sabra et al. (2005); Yao et al. (2006).

Three-station interferometry, in contrast, considers recordings from three seismic stations at a time. This method takes the cross-correlation between recordings of ambient noise at one station, which acts as a virtual source and which we call the "*source-station*", with recordings from two other stations, which are called the "*receiver-stations*". These two cross-correlations, or particular segments of them, are then cross-correlated again (or, as discussed further below, convolved). Stacking the resulting waveforms from many source-stations for the same pair of receiver-stations provides an estimate of the Green's function between the two receiver-stations. This method, therefore, is based on cross-correlations performed three at a time, where the last one has been referred to as the "correlation of correlations" (Stehly et al., 2008) but in certain circumstances will be a convolution of correlations. We refer to this method generally speaking as "*three-station interferometry*", to distinguish it from traditional two-station ambient noise methods. When the final cross-correlation is between the coda-wave parts of the first two correlations the method is commonly referred to as the "*correlation of the coda of correlations*" or C^3 (Stehly et al., 2008).

Fig. 1 illustrates some of the notation introduced in this paper. For two-station interferometry, we denote the cross-correlation between a pair of seismograms observed at stations r_i and r_j as $C_2(r_i, r_j)$. With an appropriate phase-shift, $C_2(r_i, r_j)$ can be converted to an estimate of the Green's function between the two stations, $\hat{G}_2(r_i, r_j)$, where we suppress the time-dependence of the correlations and the estimated Green's function. For three-station interferometry, cross-correlations between observations at a source-station, s_k $(1 \leq k \leq N)$, with the two receiver-stations, $C_2(s_k, r_i)$ and $C_2(s_k, r_j)$, are correlated again (or in some circumstances convolved). This produces the three-station "*source-specific interferogram*", $C_3(r_i, r_j; s_k)$, for source-station s_k, which provides information about the medium between the two receiver-stations. (The subscript "3" distinguishes the final cross-correlation or convolution from the first two correlations.) The "*composite Green's function*" for three-station interferometry is produced by taking a weighted sum over the contributing source-specific interferograms from the N source-stations:

$$\hat{G}_3(r_i, r_j) = \sum_{k=1}^{N} w_k C_3(r_i, r_j; s_k) \tag{1}$$

where w_k is a weight. For this equation to hold, C_3 must have an appropriate phase-shift applied prior to the summation.

The advantages of two-station interferometry include its simplicity and general applicability. The principal advantage of the three-station method over the two-station method is that the two receiver-stations do not have to operate at the same time, although they do have to operate synchronously with each source-station for some length of time. Thus, three-station interferometry can be applied to asynchronously deployed stations (Ma & Beroza, 2012), which provides the opportunity for what Entwistle et al. (2015) call "retrospective seismology". In terms of applications, the method will be most impactful in settings where there is a long-term backbone seismic network to provide the source-stations and shorter term deployments from which the receiver-stations are taken.

In practice, the data processing involves three noteworthy subtleties. (1) The cross-correlations of seismic noise data that form the basis for both the two-station and three-station methods involve refined data processing methods that aim to speed convergence and reduce sensitivity to earthquakes and localized persistent noise sources (e.g., Ritzwoller & Feng, 2019). We discuss the methods of data processing that we use in **sections 2 and 3** below, but we do not attempt to optimize data processing procedures for three-station interferometry.

(2) We must specify which parts of the cross-correlations of seismic noise, $C_2(s_k, r_i)$ and $C_2(s_k, r_j)$, that are correlated or convolved to produce the source-specific interferogram for source s_k, $C_3(r_i, r_j; s_k)$. **Fig. 2** identifies the two parts of the cross-correlations relevant to this study: the coda-wave (CW) and the direct-wave (DW) parts. If coda waves are correlated, we refer to the method to produce an estimated Green's function as "*coda-wave interferometry*" and if direct waves are correlated or convolved we call it "*direct-wave interferometry*".

(3) Finally, it is important to specify how to determine the weights, w_k, that convert individual source-specific interferograms to the estimated Green's function. One aspect of the choice of weights is the geometrical relationship between the receiver-stations and each source-station. For coda-wave interferometry there is no geometrical constraint so that all source-stations are used for a given receiver-station pair irrespective of their relative position; that is, the geometrical-weights are all unity (**Fig. 3a**). However, for direct-wave interferometry we impose the constraint that the source-stations lie within appropriately defined "stationary phase zones" so that sources outside those zones are given zero geometrical-weight and sources inside the zones are given unit geometrical-weight. The stationary phase zone is a Fresnel ellipse for source-stations between the receiver-stations (**Fig. 3c**) or hyperbolae for source-stations not between the receiver-stations (**Fig. 3b**), where the receiver-stations are the foci of both the ellipse and the hyperbolae. Another aspect of these weights is based on a measure of the quality of each source-specific interferogram, $C_3(r_i, r_j, s_k)$. Both aspects of assigning weights are discussed in greater detail in **section** 3.2.

It is useful to define nomenclature to distinguish the interferometric methods considered here. Traditional two-station ambient noise (AN) interferometry is denoted:

$$\mathcal{I}_2^{AN},$$

where the "2" represents the number of stations used. Three-station methods require the specification of two additional fields, "*type*" and "*geometry*", so that three-station interferometric methods are denoted generally as:

$${}^{geometry}\mathcal{I}_3^{type}.$$

Here, "type" indicates either coda-wave (CW) or direct-wave (DW) interferometry, "geometry" represents the shape of the stationary phase zone, and the "3" indicates the number of stations used in the method prior to stacking over source-stations. Of course, in the stacking of eq. (1) multiple source-stations will typically be used, but data analysis is performed three stations at a time. There is no geometrical constraint for coda-wave interferometry; thus this field is left blank in this case. For direct-wave interferometry the geometrical constraint is either an ellipse (ell) or a hyperbola (hyp).

Therefore, we identify three general methods of three-station interferometry to estimate Green's functions. First, three station coda-wave interferometry is denoted as

$$\mathcal{I}_3^{CW}.$$

Therefore, there is the following relationship between our notation and earlier notation: $\mathcal{I}_3^{CW} \equiv C^3$. Second, three-station direct-wave interferometry with sources in the elliptical stationary phase zone between the receiver-stations is represented as

$${}^{ell}\mathcal{I}_3^{DW}.$$

Finally, we indicate three-station direct-wave interferometry with sources in the hyperbolic stationary phase zones radially outside the receiver-stations as

$${}^{hyp}\mathcal{I}_3^{DW}.$$

When we refer to direct-wave interferometry generally without distinguishing between the geometry of the stationary phase zones, we will use the symbol $\mathcal{I}_3^{DW}$, leaving the geometry field blank.

Three-station coda-wave interferometry ($\mathcal{I}_3^{CW}$) was initiated by Stehly et al. (2008) and has been fairly well studied (e.g., Garnier & Papanicolaou, 2009; Froment et al., 2011; Ma & Beroza, 2012; Zhang & Yang, 2013; Entwistle et al., 2015; Haendel et al., 2016; Sheng et al., 2017, 2018; Spica et al., 2017). Applications of $\mathcal{I}_3^{CW}$ to surface wave tomography or 3-D model construction remain rare, however, in particular at regional or continental scales. To the best of our knowledge, the principal exceptions are two studies that combine group velocity measurements from $\mathcal{I}_3^{CW}$ with traditional ambient noise interferometry ($\mathcal{I}_2^{AN}$) to improve 3-D models of Mexico and the southern US (Spica et al., 2016), and of the Iranian Plateau (Ansaripour et al., 2019).

In comparison, three-station direct-wave interferometry ($\mathcal{I}_3^{DW}$) has received much less attention. Froment et al. (2011) discussed the possibility for using direct versus coda waves, and differentiated between two types of correlations of correlations: C^3_{coda} and C^3_{all}, where C^3_{coda} denotes the correlation of the coda of correlations and C^3_{all} refers to correlating the entirety of the correlations. Thus, as noted above, their C^3_{coda} is similar to our $\mathcal{I}_3^{CW}$ and because the direct-waves dominate the coda-waves in the correlations, their C^3_{all} is in some ways similar to our $\mathcal{I}_3^{DW}$. They, however, do not discuss constraining the source-stations in direct-wave interferometry to lie in stationary phase zones, although other studies do (e.g., Curtis & Halliday, 2010; Entwistle et al., 2015). Moreover, the latter studies also recognize that for the elliptical stationary phase zone, when source-stations lie generally between the receiver-stations, the original cross-correlations should be convolved with one another rather than cross-correlated. Therefore, for ${}^{hyp}\mathcal{I}_3^{DW}$ the three data operations are all cross-correlations, but for ${}^{ell}\mathcal{I}_3^{DW}$ the third data operation is a convolution. Discussion of the role of convolution in interferometry goes back at least to Slob and Wapenaar (2007). Entwistle et al. (2015) applied aspects of direct-wave interferometry to data from the EarthScope Transportable Array, but to the best of our knowledge $\mathcal{I}_3^{DW}$ has not yet been applied tomographically or in the context of inversions for 3-D models and its properties remain poorly understood.

The purpose of this paper is to determine and compare empirically the characteristics of the three-station methods to each other and to two-station interferometry. From the outset, it is evident that coda-wave interferometry has the advantage that any geometrical relationship can exist between the source-stations and the receiver-stations, whereas for direct-wave interferometry only a small subset of stations can be used as source-stations for each pair of receiver-stations. In coda-wave interferometry, however, signals emerge very slowly with the addition of source-stations, which means that many more source-stations are needed to recover reliable estimated Green's functions. Therefore, the relative merits of direct-wave interferometry and coda-wave interferometry (which of the methods will be preferable, in what ways, and in which settings) need to be determined empirically.

We address these questions by applying $\mathcal{I}_2^{AN}, \mathcal{I}_3^{CW}, {}^{ell}\mathcal{I}_3^{DW}$, and ${}^{hyp}\mathcal{I}_3^{DW}$ across the central and western US to all stations west of 95°W longitude from the EarthScope Transportable Array to measure Rayleigh wave dispersion from 8 s to 80 s period and present associated phase speed maps from 10 s to 60 s period. We pay particular attention to the agreement between the three-station results and the two-station results, including systematic differences (bias) and fluctuation, and to the distributions of measurements as functions of signal-to-noise ratio (SNR), band-width, and the number of measurements produced for asynchronously deployed receiver-stations.

2 Data

Three-station interferometry ($\mathcal{I}_3$) is based on data output from two-station interferometry ($\mathcal{I}_2$). As the basis for the three-station interferometry in this study, we use the two-station database of ambient noise cross-correlations (C_2) constructed by Shen and Ritzwoller (2016). Stations in the database of Shen and Ritzwoller (2016) extend across the contiguous US, but we use only a subset of them in the central and western US (west of 95°W longitude), which defines our region of study (**Fig. 4**). We use all 1047 EarthScope USArray stations in this region deployed from 2005 to 2010, including 979 Transportable Array (_US-TA) stations and 68 Reference Network (_US-REF) stations. We retain a two-station cross-correlation only if its signal-to-noise ratio (SNR) is greater than 10, where SNR is defined as the ratio of the maximum amplitude of the waveform in the direct-wave time window to the root-mean square of the waveform in the coda-wave window (**Fig. 2**). SNR defined in this way is independent of frequency. Among the 547,581 possible combinations of pairs from the 1047 stations, 66% (364,103) operated synchronously so that two-station ambient noise interferometry could be employed. Of these, we retained 325,446 (89%) cross-correlations that met the SNR criterion. In contrast, 34% (183,478) of the station-pairs were deployed asynchronously.

The deployment of the Transportable Array started from the West Coast and rolled eastward, with stations deployed temporarily for ∼2 years (**Fig. 4**). This rolling pattern provides an ideal geometry for direct-wave interferometry with an elliptical stationary phase zone, ${}^{ell}\mathcal{I}_3^{DW}$, in which source-stations lie approximately between receiver-stations. In contrast, the Reference Network was deployed permanently and was scattered across the US with a station spacing of ∼300 km. This is a good geometry for coda-wave interferometry, $\mathcal{I}_3^{CW}$, and direct-wave interferometry with a hyperbolic stationary phase zones, ${}^{hyp}\mathcal{I}_3^{DW}$, in which source-stations lie approximately radially outward from receiver-stations.

Shen and Ritzwoller (2016) used a common method of ambient noise data processing (Bensen et al., 2007). Briefly, continuous records of vertical component seismograms are cut to day-long segments and downsampled from 40 Hz to 1 Hz. Then the instrument response, mean and trend are removed. To minimize the effects of strong directional sources (in particular earthquakes) and to broaden the usable bandwidth, temporal normalization and spectral whitening are applied. The temporal normalization uses a 80 s running time window, which strongly attenuates signals with periods above 80 s. For this reason we will focus our interpretation on measurements only up to 80 s period and show tomographic results only up to 60 s period.

After pre-processing, daily seismograms from all available combinations of station-pairs (r_i, r_j) are cross-correlated to produce $C_2(r_i, r_j)$, between correlation lag times of ± 3000 s. Daily correlations are then stacked to generate two-station estimated Green's functions between each pair of stations $(\hat{G}_2(r_i, r_j))$. Finally, we compute the so-called "symmetric component" of the estimated Green's function by averaging the estimated Green's function at positive and negative correlation lags for simplicity. We will also refer to this symmetric component estimated Green's function as $\hat{G}_2(r_i, r_j)$, even though it is defined only for positive lag. This database of symmetric component estimated Green's functions is the basis for the three-station analysis (**section 3**).

3 Data Processing for Three-Station Interferometry

The input for three-station interferometry are the two-station symmetric component cross-correlations (or estimated Green's functions) taken from the database of Shen and Ritzwoller (2016) with SNR > 10. As inter-station cross-correlations, these functions are denoted by C_2 and as estimated Green's functions by $\hat{G}_2$. Three-station source-specific interferograms (C_3) are cross-correlations of the coda-wave parts of the inter-station cross-correlations, or cross-correlations or convolutions of the direct-wave parts of the inter-station cross-correlations. Three-station data processing aims to compute the composite Green's function between pairs of receiver-stations by stacking the three-station interferograms over contributions from various source-stations.

For concreteness, consider a receiver-station pair (r_i, r_j) and a set of source-stations, $\{s_k\}_{k=1}^{N}$, that operate synchronously with both r_i and r_j at least for some time. **Fig. 1b** depicts this situation, where one source-station is shown. Let the coda-wave parts of the two-station cross-correlations be denoted $C_2^{CW}(s_k, r_i)$ and $C_2^{CW}(s_k, r_j)$, and the direct-wave parts be written $C_2^{DW}(s_k, r_i)$ and $C_2^{DW}(s_k, r_j)$, where the coda-wave and direct-wave segments are defined in **Fig. 2**. The three-station data processing procedure breaks into three principal steps (**sections 3.1 - 3.3**).

3.1 Construcing Source-Specific Interferograms

The first step in three-station data processing is devoted to cross-correlating or convolving segments of the two-station cross-correlations. It is broken into three categories depending on whether one considers the direct- or coda-wave segments of the two-station cross-correlations and the geometrical relationship between the receiver-station pair and each source-station. For direct-waves, the geometrical relationship is summarized in terms of hyperbolic or elliptical stationary phase zones (**Fig. 3b,c**).

(1) The first category is, for each source-station, to compute the three-station source-specific interferograms based on the coda-waves in the two-station cross-correlations. That is, correlate $C_2^{CW}(s_k, r_i)$ and $C_2^{CW}(s_k, r_j)$ for all s_k to produce $C_3^{CW}(r_i, r_j; s_k)$ for $1 \leq k \leq N$. An example record-section containing three-station coda-wave source-specific interferograms is presented in **Fig. 5a**, where each trace is for a separate source-station.

(2) The second category is to compute the three-station source-specific interferograms based on the direct-waves in the two-station cross-correlations for the source-stations in the hyperbolic stationary phase zones. For each source-station s_k in the stationary-phase hyperbolae for the receiver-station-pair, cross-correlate $C_2^{DW}(s_k, r_i)$ and $C_2^{DW}(s_k, r_j)$ to produce ${}^{hyp}C_3^{CW}(r_i, r_j; s_k)$. An example record-section for three-station direct-wave source-specific interferograms computed by cross-correlation is shown in **Fig. 5b**, where each trace is for a separate source-station. For this record-section, cross-correlations are computed based on source-stations irrespective of whether they lie in the stationary-phase hyperbolae. However, the green-shaded regions identify the stationary phase zones.

(3) The third category is similar to the second, but we compute the three-station source-specific interferograms based on the direct-waves in the two-station cross-correlations for the source-stations in the elliptical stationary phase zone. For each source-station s_k in the stationary-phase ellipse for this receiver-station-pair, convolve the direct-wave parts of $C_2(s_k, r_i)$ and $C_2(s_k, r_j)$ to produce ${}^{ell}C_3^{CW}(r_i, r_j; s_k)$. An example record-section for three-station source-specific direct-wave interferograms computed by convolution is shown in **Fig. 5c**, where each trace is for a separate source-station. As in **Fig. 5b**, convolutions are presented irrespective of whether the source-station lies in the stationary-phase ellipse, but the green-shaded region identifies the stationary phase zone.

Convolution of the direct-wave parts of the two-station records when source-stations lie in the elliptical stationary phase zone has been formally justified by other studies (e.g., Halliday & Curtis, 2009; Curtis & Halliday, 2010). We provide a heuristic argument for illumination. When a source-station lies radially outward from a pair of receiver-stations, it is the time-difference between the travel times from the source-station to the two receiver-stations that approximates the travel time between the two receiver-stations. Cross-correlation of two records finds the time-difference between them, therefore when source-stations lie outside the receiver-stations it is the appropriate method to apply. In contrast, convolutions find the sum of the times. When a source-station lies between two receiver-stations, we wish to find the sum of the times from the source-station to each receiver-station, so that convolution is the appropriate method to apply in this case.

Both the hyperbolic and elliptical stationary phase zones are straightforward to define. An ellipse is defined as the locus of points where the sum of the distances to the foci is constant. Let d_{ij} be the great-circle distance between the two receiver-stations, d_{ki} be the distance between a point s_k on the ellipse and receiver-station r_i, and d_{kj} be the distance between s_k and receiver-station r_j. Then we define the elliptical stationary phase zone for method ${}^{ell}\mathcal{I}_3^{DW}$ as

$$d_{ki} + d_{kj} \leq (1+\alpha)d_{ij}, \tag{2}$$

where $\alpha \geq 0$ and we choose $\alpha = 10^{-2}$. Thus, if source-station s_k lies within the elliptical stationary phase zone, the sum of distances from s_k to r_i and to r_j is less than 1% longer than the distance between the receiver-stations.

Similarly, a hyperpola is defined as the locus of points where the difference of the distances to the foci is constant. We therefore define the hyperbolic stationary phase zones for method ${}^{hyp}\mathcal{I}_3^{DW}$ as

$$|d_{ki} - d_{kj}| \geq (1-\alpha)d_{ij}, \tag{3}$$

where $\alpha \in [0,1]$ and again we choose $\alpha = 10^{-2}$. This means that if source-station s_k lies within the hyperbolic stationary phase zone, the difference of distances from s_k to r_i and to r_j is greater than 99% of the distance between the receiver-stations. On a sphere, the locus of points where the difference of the distances to the foci is constant, however, approximates a hyperbola only near the foci.

The stationary phase zones can be defined alternatively using azimuthal angle θ (**Fig. 3**) instead of α. For the methods $\mathcal{I}_3^{CW}$ and ${}^{hyp}\mathcal{I}_3^{DW}$, θ is the angle from the source-station to the mid-point between the receiver-stations (**Fig. 3a,b**), which defines the slopes of the asymptotes of a hyperbola. It is related to α by $\cos\theta = 1-\alpha$, where $\theta \in [0, 2\pi]$. The definition of angle θ for a given source-station for method ${}^{ell}\mathcal{I}_3^{DW}$ is motivated by the symmetry in eqs. (4) and (5) below. To do so, first identify the ellipse on which the source-station lies with the two receiver-stations as foci. Then find the intersection point between the ellipse and the perpendicular bisector of the line segment linking the two receiver-stations. Angle θ is the angle between a receiver-station and this intersection point. **Fig. 3c** shows an example of this intersection point, but does not identify the location of the source-station or the ellipse on which it lies. In this case, θ is related to α by $\cos\theta = 1/(1+\alpha)$, where $\theta \in [0, \frac{\pi}{2}]$. For the same α, θ is generally larger for ${}^{hyp}\mathcal{I}_3^{DW}$ than for ${}^{ell}\mathcal{I}_3^{DW}$. Our choice of $\alpha = 10^{-2}$ corresponds to a maximum $\theta \approx 8°$ for both ${}^{hyp}\mathcal{I}_3^{DW}$ and ${}^{ell}\mathcal{I}_3^{DW}$.

We use eqs. (2) and (3) with $\alpha = 10^{-2}$ to define the stationary phase zones in this paper for methods ${}^{ell}\mathcal{I}_3^{DW}$ and ${}^{hyp}\mathcal{I}_3^{DW}$, respectively. These definitions are chosen for simplicity and because they appear to provide reliable results in the applications we consider. However, the choice of the value of α is ad-hoc as is its frequency-independence. More elaborate, perhaps frequency-dependent, definitions may prove to be preferable.

The approximate arrival time, δt, for method ${}^{hyp}\mathcal{I}_3^{DW}$ is known (e.g., Yao & van der Hilst, 2009):

$$\delta t = \frac{d_{ij}}{v}\cos\theta, \tag{4}$$

for a plane-wave in a medium with constant wave speed v, where d_{ij} is the inter-receiver-station distance and θ is shown in **Fig. 3b**. The grey line plotted in **Fig. 5b** is for this formula. Analogously, the approximate arrival time t_{sum} for method ${}^{ell}\mathcal{I}_3^{DW}$ is:

$$t_{sum} = \frac{d_{ij}}{v}\sec\theta, \tag{5}$$

for θ shown in **Fig. 3c**. The grey line plotted in **Fig. 5c** is for this formula.

3.2 Stacking Weights

Appropriate stacking weights w_k must be computed for each source-station s_k for each of the three-station methods ($\mathcal{I}_3^{CW}$,${}^{hyp}\mathcal{I}_3^{DW}$ and ${}^{ell}\mathcal{I}_3^{DW}$) to compute the composite Green's functions. The principal weight that we use is to set w_k equal to the reciprocal of the root-mean-square (rms) of the noise in the coda-wave part of each source-specific interferogram, $C_3(r_i, r_j; s_k)$ for receiver-stations r_i and r_j. Defined in this way, we down-weight each contributing cross-correlogram by the rms of trailing noise. We do not, however, normalize the amplitude of the cross-correlograms. Therefore, down-weighting by the rms of trailing noise is approximately equivalent to normalizing the amplitudes of the cross-correlograms then weighting by peak signal-to-rms trailing noise ratio (SNR). Because the peak signal grows approximately linearly with the time series length of the records used to compute the cross-correlations, and rms trailing noise grows approximately as the square root of the time series length, SNR grows approximately as the square root of time series length (e.g., Snieder, 2004; Bensen et al., 2007). Thus, the use of this weighting scheme tends to accentuate the contribution from longer cross-correlations, but less strongly than if we had not normalized by peak amplitude and inversely by the rms of the trailing noise.

There are three other aspects of the data processing that can be considered to be stacking weights. First, for the direct-wave three station methods, we only include a source-station in the stack if it lies within an appropriately defined stationary phase zone, which is referred to as geometrical-weighting in the Introduction. This choice can be thought of as applying binary weights to source-stations depending on their position relative to the receiver-stations. Second, also as mentioned above, unless the two constituent two-station interferograms, $C_2(s_k, r_i)$ and $C_2(s_k, r_j)$, both have SNR ≥ 10, the weight of the corresponding three-station interferogram, $C_3(r_i, r_j; s_k)$, is set to zero; otherwise it is unity. Third, for the coda-wave three station method, a source-station is excluded if the length of either $C_2^{CW}(s_k, r_i)$ or $C_2^{CW}(s_k, r_j)$ is less than 1500 s, which is needed to include signals for the longest station pairs (> 3000 km).

3.3 Estimating Composite Green's Functions

To compute the composite Green's function, $\hat{G}(r_i, r_j)$, for each of the three-station methods we apply the weighted sum given by eq. (1) based on the stacking weights (section 3.2). **Fig. 6** provides some examples using the same pair of receiver-stations used in the record-sections of **Fig. 5**. s **Fig. 6a** presents an example composite Green's function for three-station coda-wave interferometry ($\mathcal{I}_3^{CW}$). For this method, no stationary phase zone is needed, so contributions from all source-stations are included in the stack. This is the black line in **Fig. 6a**, labelled "stack all", which is compared to the two-station ambient noise cross-correlation plotted as the red line and labelled $\mathcal{I}_2^{AN}$. Two observations of noteworthy: First, one of the features of coda-wave interferometry is the tendency for the composite Green's functions to be more symmetric than for two-station ambient noise methods (e.g., Stehly et al., 2008, and many others), and this is also observed in this example. We found it, however, to be an artifact due to the use of symmetric components (Sheng et al., 2018). Second, the SNR of the three-station coda-wave composite Green's function is lower than for the two-station record, even though in this case 514 source-stations contribute to the three-station interferogram. This highlights another aspect of coda-wave interferometry, i.e., signals emerge from noise very slowly as source-stations are introduced. And, as can be seen in **Fig. 5a**, constituent source-specific three-station interferograms are typically very noisy so that signals cannot be discerned in any of them. The implication is that coda-wave interferometry can play a useful role in ambient noise interferometry only in the presence of many long duration source-stations, unless more sophisticated data processing procedures are applied (**section 6.2**). For comparison, we also plot in **Fig. 6a** the recovered composite Green's function based on source-stations that lie exclusively in the hyperbolic stationary phase zone. The choice of source-stations in this zone further degrades the SNR of the composite Green's function, indicating that there is no geometrical advantage to choosing source-stations in the end-fire directions in coda-wave interferometry.

Fig. 6b shows an example composite Green's function for three-station direct-wave interferometry where the source-stations lie in the hyperbolic stationary phase zone (${}^{hyp}\mathcal{I}_3^{DW}$). In this case, the green line, which is the stack for source-stations only in the hyperbolic stationary phase zones (labelled "stack in hyp"), is the Green's function estimate, and there are 26 source-stations. Retaining source-stations at all azimuths (black line) degrades the result by adding precursory noise. Two comments are worthy of note in comparing the three-station composite Green's function (green line) with two-station Green's function (red line). First, the relative amplitudes for the different correlation lags are more similar than for coda-waves. Second, precursory noise is lower for the three-station estimate. These are both common characteristics when comparing two-station to three-station Green's functions.

Finally, **Fig. 6c** presents an example composite Green's function for three-station direct-wave interferometry where the source-stations lie in the elliptical stationary phase zone (${}^{ell}\mathcal{I}_3^{DW}$). The green line, which is the stack for source-stations only in the eliiptical stationary phase zones (labelled "stack in ellipse"), is the composite Green's function estimate, and there are 7 source-stations. As with the hyperbolic stationary phase zone, retaining source-stations at all azimuths (black line) degrades the result but in this case adds both precursory and trailing noise, especially the latter. In this case, too, there is lower precursory noise for the three-station estimate than for $\mathcal{I}_2^{AN}$.

4 Dispersion Measurements

As part of dispersion measurement, we apply two additional quality control criteria. First, for a dispersion measurement to be retained, we apply a spectral SNR (Bensen et al., 2007) criterion to the composite Green's function, where again SNR is defined as the peak amplitude in the direct-wave window divided by the rms of the waveform in the coda-wave window. That is, at a given period the SNR of the composite Green's function must be ≥ 10 or else the dispersion measurement at that period is discarded. Second, for the dispersion measurement to be retained, the distance between the two receiver-stations must be greater than one wavelength. For example, if the phase speed is 3.5 km/s, at 20 s period the receiver-stations must be separated by more than 70 km. This criterion becomes more restrictive as period increases. We do not, however, apply the one-wavelength criterion to the two source-receiver cross-correlations.

To measure frequency dependent phase speed, we apply frequency-time analysis (FTAN; Dziewonski et al., 1969; Levshin & Ritzwoller, 2001; Bensen et al., 2007). We assume that the measured phase of a seismogram at frequency ω in the frequency domain for receiver-stations r_i and r_j is approximately (Lin et al., 2008)

$$\phi_{ij}(\omega) = \frac{\omega}{c_{ij}} d_{ij} + \frac{\pi}{4} + 2N\pi + \phi_s, \ N \in \mathbb{Z}, \tag{6}$$

where d_{ij} is the distance between the two receiver-stations, $\pi/4$ is from the far-field or high-frequency asymptotic approximation of the Bessel function, ϕ_s is an initial phase term, and c_{ij} is the frequency-dependent phase speed, which is what we aim to measure. A key assumption here is that we use the inter-receiver-station distance in eq. (6). This assumption leads to a biased measurement for the three-station direct-wave methods, and the nature of this bias and its correction is discussed in **sections 5.3** and 6.1.

For two-station ambient noise interferometry, $\mathcal{I}_2$, $\phi_s \approx 0$ has been shown theoretically (e.g., Snieder, 2004) and empirically (e.g., Yao et al., 2006; Lin et al., 2008). For three-station coda-wave interferometry, $\mathcal{I}_3^{CW}$, ϕ_s should also be approximately 0. However, for three-station direct-wave interferometry, $\mathcal{I}_3^{DW}$, ϕ_s will differ from 0, and this initial phase must be taken into account when measuring phase speed. Because correlation or convolution of two composite Green's functions will determine the difference or sum of the phases in the frequency domain, respectively:

$$\phi_s \approx \begin{cases} \frac{\pi}{4} & \text{for } {}^{ell}\mathcal{I}_3^{DW}, \\ -\frac{\pi}{4} & \text{for } {}^{hyp}\mathcal{I}_3^{DW}. \end{cases} \quad (7)$$

The use of these values of ϕ_s for $\mathcal{I}_3^{DW}$ is tested in **section 5**.

Fig. 7 compares example frequency-time (FTAN) diagrams for the two-station method and the three-station methods, for the two receiver-stations M07A and M15A. The four diagrams are similar but the diagrams for the two direct-wave methods show larger relative amplitudes at longer periods and the coda-wave diagram has group speeds that increase non-physically at longer periods. A detailed comparison of the dispersion measurements that emerge from the various methods is presented in **section 5.2**.

5 Results

To validate and compare the three-station methods we report results from the raw dispersion measurements and from surface wave tomography based on them. To perform tomography, we apply the eikonal tomography method (e.g., Lin et al., 2009) to Rayleigh wave phase speed measurements obtained from the two-station and three-station methods. We employ the eikonal tomography method rather than traditional tomographic methods that minimize a penalty functional (e.g., Barmin et al., 2001) because eikonal tomography applies no ad-hoc regularization that depends on data coverage. This simplifies comparison of results from different datasets because they are less affected by differences in the number and distribution of wave paths.

5.1 General Characteristics of $\mathcal{I}_3$ Measurements

Fig. 8a summarizes the spectral signal-to-noise ratio (SNR) of each of the four interferometric methods, averaging over the entire data set of dispersion measurements. Generally speaking, SNR decreases with period and the trends are similar between $\mathcal{I}_3$ and $\mathcal{I}_2^{AN}$. The peak near 20 s periods corresponds to the primary microseism, while the dip near 26 s period corresponds to the existence of a spatially localized microseismic source (e.g., Shapiro et al., 2006). **Fig. 8b** presents the SNR results relative to the SNR for $\mathcal{I}_2^{AN}$. The SNR for ${}^{ell}\mathcal{I}_3^{DW}$ is slightly larger than for ${}^{hyp}\mathcal{I}_3^{DW}$, while both have a SNR more than twice that of $\mathcal{I}_2^{AN}$ across a broad bandwidth. In contrast, $\mathcal{I}_3^{CW}$ has a much lower median SNR (< 10) across all periods.

Because SNR plays the most significant role in the quality control of dispersion measurements, the number of accepted $\mathcal{I}_2$ and $\mathcal{I}_3$ measurements varies with period similar to SNR (**Fig. 9a**). The number of accepted $\mathcal{I}_3$ measurements can be divided into three categories depending on whether the two receiver-stations operated at the same time (synchronously) and whether an $\mathcal{I}_2$ measurement exists for the path so that the $\mathcal{I}_3$ measurement is new or repeated. These three categories of $\mathcal{I}_3$ measurements are referred to as "Synchronous-Repeated" (receiver-stations deployed synchronously, with both an $\mathcal{I}_3$ and an $\mathcal{I}_2$ measurement), "Synchronous-New" (receiver-stations deployed synchronously, with an $\mathcal{I}_3$ but not an $\mathcal{I}_2$ measurement), and "Asynchronous-New" (receiver-stations deployed asynchronously, with only an $\mathcal{I}_3$ measurement). In the Synchronous-New case, the receiver-stations produced an $\mathcal{I}_2$ measurement but it was rejected, usually because it did not meet the SNR requirement. The numbers of $\mathcal{I}_3$ measurements that derive from these three categories are shown in **Fig. 9b-d**. In all categories, ${}^{ell}\mathcal{I}_3^{DW}$ measurements somewhat outnumber the ${}^{hyp}\mathcal{I}_3^{DW}$ measurements, and both outnumber the $\mathcal{I}_2^{AN}$ measurements (in cases where they exist) and greatly outnumber the $\mathcal{I}_3^{CW}$ measurements.

Fig. 9b is for the Synchronous-Repeated category of $\mathcal{I}_3$ measurements. By definition, the number of $\mathcal{I}_3$ measurements will be no larger than the number of $\mathcal{I}_2$ measurements. Nearly every existing $\mathcal{I}_2^{AN}$ measurement is accompanied by an $\mathcal{I}_3^{DW}$ measurement, but the number of $\mathcal{I}_3^{CW}$ measurements is considerably smaller. The number of these measurements generally decreases with period after maximizing between 20 and 30 s, although the $\mathcal{I}_3^{CW}$ measurement maximizes nearer to 15 s period and decays very rapidly at longer periods.

Fig. 9c is for the Synchronous-New category of $\mathcal{I}_3$ measurements, and illustrates that many new longer periods measurements emerge from the $\mathcal{I}_3^{DW}$ method. Above about 50 s period, $\mathcal{I}_3^{DW}$ nearly doubles the number of measurements between synchronously deployed stations. Although a principal attraction of the three-station methods is the ability to obtain measurements between asynchronously deployed stations, but many new measurements result from the $\mathcal{I}_3^{DW}$ methods even for synchronously deployed stations particularly at long periods. There are essentially no new measurements from $\mathcal{I}_3^{CW}$ in this category.

Fig. 9d is for the Aynchronous-New category of $\mathcal{I}_3$ measurements, measurements from the $\mathcal{I}_3$ methods that are inherenently non-existent for $\mathcal{I}_2$. Relative to the number of measurements delivered by $\mathcal{I}_2^{AN}$, the greatest impact of the $\mathcal{I}_3$ methods is at the longer periods of the bandwidth considered. The vast majority of the measurements for $\mathcal{I}_3^{CW}$ are from synchronously deployed stations (**Fig. 9b**), indicating that it is difficult for $\mathcal{I}_3^{CW}$ to bridge asynchronous stations.

5.2 Phase Speed Measurements from Three-Station ($\mathcal{I}_3$) vs. Two-Station ($\mathcal{I}_2$) Interferometry

Fig. 10 and **Table 1** present comparisons of Rayleigh wave phase speed measurements derived from the three-station methods to two-station interferometry for common receiver-station pairs. Let $\hat{G}_3(r_i, r_j)$ be a composite three-station Green's function between receiver-stations r_i and r_j, and $\hat{G}_2(r_i, r_j)$ be the two-station estimate of the Green's function between the same two stations, where the time-dependence is suppressed in this notation. **Fig. 10** and **Table 1** present the mean and standard deviation of the difference between $\hat{G}_3(r_i, r_j)$ and $\hat{G}_2(r_i, r_j)$ computed over all common receiver-station pairs for each of the three-station methods.

Fig. 10a and **Table 1** (column 2) show that the mean difference between the two-station Green's functions and the three-station composite Green's functions based on coda-waves is negligible (< 1 m/s, on average), from which we infer that the three-station method based on coda-waves is unbiased. The standard deviation of the difference grows with period, but is small (< 15 m/s) at all periods, although results extend only up to 22 s period.

In contrast, **Fig. 10b,c** and **Table 1** (columns 4 & 6) show the existence of a non-zero systematic difference or bias between each of the three-station direct-wave methods and two station interferometry. For ${}^{ell}\mathcal{I}_3^{DW}$, the absolute amplitude of the bias generally increases with period (from less than 10 m/s at 10 s to nearly 20 m/s at 80 s). For ${}^{hyp}\mathcal{I}_3^{DW}$, the absolute amplitude of the bias increases with a similar trend until 40 s, but then decreases rapidly (to only 1 m/s at 80 s). For the reasons discussed in **section 6.1**, ${}^{ell}\mathcal{I}_3^{DW}$ is biased slow relative to $\mathcal{I}_2^{AN}$ (the difference in **Fig. 10b** is negative on average) and ${}^{hyp}\mathcal{I}_3^{DW}$ is biased fast (the difference in **Fig. 10c** is positive on average). We also discuss in **section 6.1** a ray-theoretic approach to reducing this bias.

In contrast with the bias, the standard deviations of the differences between the dispersion measurements from the $\mathcal{I}_2^{AN}$ method to both $\mathcal{I}_3^{DW}$ methods grow with period, as **Fig. 10b,c** and **Table 1 (columns 5 & 7)** show, particularly above 40 s period. Partly, this is due to the decrease in signal-to-noise ratio (SNR) in both the three-station and two-station Green's functions at longer periods (**Fig. 9a**). However, irrespective of SNR, we do not expect the dispersion measurements from the three-station methods to agree with those from the two-station method as well at longer periods. The reason is that the Fresnel Zone or sensitivity kernel for the three-station methods is not identical to the sensitivity kernel for the two-station method and the differences in sensitivity grow with period.

Fig. 11 schematically illustrates the difference in sensitivity for the three-station direct-wave measurements and the two-station measurement, in which we approximate the Fresnel Zone for the two-station method as an ellipse, shown with dashed lines, with the two receiver-stations at the ellipse's foci. The Fresnel Zone for the method ${}^{ell}\mathcal{I}_3^{DW}$ is approximately the sum of the two Fresnel zones for each of the constituent waves that emanate from the source-station (red dot in **Fig. 11a**) which lies between the receiver-stations for this method. The sensitivity zone for ${}^{ell}\mathcal{I}_3^{DW}$ is smaller than for $\mathcal{I}_2$, on average, and we therefore expect that the method ${}^{ell}\mathcal{I}_3^{DW}$ will have a higher resolution than $\mathcal{I}_2$, everything else being equal. In contrast, the Fresnel Zone for the method ${}^{hyp}\mathcal{I}_3^{DW}$ is approximately the difference of the two Fresnel zones for each of the constituent waves that emanate from the source-stations (red dots in **Fig. 11b**), which lie outside the receiver-stations. This sensitivity zone for ${}^{hyp}\mathcal{I}_3^{DW}$ is larger and considerably more complicated than for $\mathcal{I}_2$, on average. We, therefore, expect that the method ${}^{hyp}\mathcal{I}_3^{DW}$ will have a lower resolution than $\mathcal{I}_2$, everything else being equal.

The Fresnel zones for the $\mathcal{I}_2^{AN}$ method widen with period, as will those for the $\mathcal{I}_3^{DW}$ methods. Therefore, differences between the Fresnel zones of the $\mathcal{I}_3^{DW}$ methods compared with the Fresnel zone of the $\mathcal{I}_2^{AN}$ method will increase with period, too, as the various methods sample the earth between and around the pair of receiver-stations increasingly differently. We believe this is the source of the increase in the standard deviations of the differences between the phase speed measurements for the various methods, as shown in **Fig. 10** and **Table 1**.

The analysis of Fresnel Zones presented here is schematic and illustrative. The Fresnel Zones have internal structure that will produce details in the sums and differences presented in **Fig. 11**. General conclusions about the nature of the differences between the various Fresnel Zones are robust, but to use this information quantitatively to improve images in the future will require much more careful computation of the Fresnel zones (e.g., de Vos et al., 2013; Fichtner et al., 2017).

5.3 Tomography Based on Three-Station ($\mathcal{I}_3$) vs. Two-Station ($\mathcal{I}_2$) Interferometry

The Rayleigh wave phase speed maps produced by the three-station ($\mathcal{I}_3$) and two-station ($\mathcal{I}_2^{AN}$) methods are generally quite similar, as displayed at periods of 10 s, 20 s, 40 s, and 60 s in **Figs 12 - 14**. The touchstone is the two-station map ($\mathcal{I}_2^{AN}$), and at each period there is substantial agreement between the $\mathcal{I}_3$ maps with the $\mathcal{I}_2^{AN}$ map. However, we do not show the three-station coda-wave ($\mathcal{I}_3^{CW}$) maps at periods of 40 s and 60 s because the method does not provide enough measurements to perform tomography reliably at periods above 25 s. Presumably, this is because the coda is enriched at the shorter periods. The number of measurements produce by each of the three-station methods is discussed in greater detail in **section 5.1**.

A more careful comparison of the tomographic maps requires detailed inspection of the differences between the maps. Let us assume that we have two dispersion maps on the same grid of longitudes (x_i) and latitudes (y_j): $c_{ij}^{(1)} = c^{(1)}(x_i, y_j)$ and $c_{ij}^{(2)} = c^{(2)}(x_i, y_j)$. Let Δ_{ij} be the difference between these maps:

$$\Delta_{ij} = c_{ij}^{(1)} - c_{ij}^{(2)}, \tag{8}$$

whose mean over (x_i, y_j) is denoted as $\bar{\Delta}$ and standard deviation as σ_Δ. **Figs 15 - 16** display such differences between the three-station methods with two-station interferometry in map form and **Table 2** summarizes the differences, tabulating $\bar{\Delta}$ and σ_Δ.

Fig. 15 (and **Table 2**, column 2) shows the difference between the Rayleigh wave phase speed maps at periods of 10 s and 20 s from three-station coda-wave interferometry ($\mathcal{I}_3^{CW}$) and two-station interferometry ($\mathcal{I}_2^{AN}$). There is essentially no systematic difference between the maps ($|\bar{\Delta}| < 1$ m/s) and the standard deviation of the differences is also small ($\sigma_\Delta < 8$ m/s). Unfortunately, we are unable to produce meaningful tomographic maps from $\mathcal{I}_3^{CW}$ at longer periods, while it may be more feasible to push $\mathcal{I}_3^{CW}$ towards shorter periods (**section 6.2**).

Fig. 16 presents difference maps at periods from 10 s to 60 s for the two three-station direct-wave methods (${}^{ell}\mathcal{I}_3^{DW}$ and ${}^{hyp}\mathcal{I}_3^{DW}$) relative to $\mathcal{I}_2^{AN}$. **Table 2**, columns 4-7, summarizes the mean and standard deviation of the difference over the maps. Both methods result in a systematic bias compared to $\mathcal{I}_2^{AN}$, albeit with different signs and the bias for ${}^{ell}\mathcal{I}_3^{DW}$ is larger than for ${}^{hyp}\mathcal{I}_3^{DW}$. In addition, the standard deviation of the differences generally grow with period. These results are similar to the bias and standard deviation in the raw phase speed measurements for the two methods (**Fig. 10** and **Table 1**). The methods produce systematic errors (or bias) for reasons that are discussed in **section 6.1**. The standard deviations of the differences grow with period because the $\mathcal{I}_3^{DW}$ methods increasingly sample the earth differently than the ($\mathcal{I}_2^{AN}$) method at longer periods (**section 5.2**).

6 Discussion

We have focused assessment of the three-station methods on the consistency between Rayleigh wave phase speed measurements and maps (tomograms) that derive from the various methods from 10 s to 60 s period (e.g., **Figs 12** - **14**). As shown, the phase speed measurements and the tomographic maps from the $\mathcal{I}_3$ methods are generally consistent with those from $\mathcal{I}_2^{AN}$. The three-station method based on coda-waves ($\mathcal{I}_3^{CW}$) has a much lower SNR than the direct-wave three-station methods as well as two-station interferometry, and produces sufficient measurements for tomography only at shorter periods ($<$ 25 s). In contrast, the three-station direct-wave methods ($\mathcal{I}_3^{DW}$) have a SNR two to three times larger than two-station interferometry ($\mathcal{I}_2^{AN}$), on average. Combining this with the bridging of asynchronous stations to provide new inter-station paths for tomography, there is as much as a factor of two enhancement relative to two-station interferometry in the number of paths across a broad frequency band. This enhancement is most prominent at longer periods ($>$40 s).

The direct-wave three-stations methods, however, possess a systematic bias relative to the $\mathcal{I}_2^{AN}$ method. The practitioner of these methods must determine whether the extent of the bias is significant for the applications of interest. For applications in which the bias is problematic, we show in **section 6.1** that the bias can be estimated and accounted for approximately with a ray-theoretic de-biasing adjustment to the dispersion measurements that is effective in the period range where ray-theory is accurate. **Section 6.2** discusses other variants of the methods presented here that may provide fruitful directions for future improvement.

6.1 Correcting the Bias in Three-Station Direct-Wave Interferometry ($\mathcal{I}_3^{DW}$)

As described above, the three-station methods are based on measuring the phase speed of the composite Green's function (equation (1)), $\hat{G}(r_i, r_j)$, between a pair of receiver-stations (r_i, r_j), which is a stack of source-specific interferograms, $C_3(r_i, r_j; s_k)$, that emerge from particular source-stations s_k. The phase speed, c_{ij}, is measured using the composite Green's function based on eq. (6) under the assumption that the appropriate propagation distance is d_{ij}, the great-circle distance between r_i and r_j. It is this assumption of d_{ij} for the composite Green's function that produces the systematic bias in the three-station direct-wave methods.

The physical cause of the bias of the three-station direct-wave methods is geometrical and can be understood ray theoretically (**Fig. 17**). For the direct-wave method based on an elliptical stationary phase zone, ${}^{ell}\mathcal{I}_3^{DW}$, the source-station s_k lies generally between the two receiver-stations at distances d_{ki} from r_i and d_{kj} from r_j (**Fig. 17a**). The actual distance the rays will travel for the method ${}^{ell}\mathcal{I}_3^{DW}$ based on source s_k is the sum of the constituent ray paths:

$$ {}^{ell}d'_{ij} = d_{ki} + d_{kj} \geq d_{ij}. \tag{9} $$

Because ${}^{ell}d'_{ij}$ is longer than the inter-receiver-station distance, assuming the distance traveled is d_{ij} will result in a phase speed that is biased slow. Similarly, for the three-station direct-wave method, ${}^{hyp}\mathcal{I}_3^{DW}$, sources lie generally outside the two receiver-stations (**Fig. 17b**). The actual distance the rays will travel for the method ${}^{hyp}\mathcal{I}_3^{DW}$ based on source s_k is the difference in the constituent ray paths:

$$ {}^{hyp}d'_{ij} = d_{ki} - d_{kj} \leq d_{ij}. \tag{10} $$

Because ${}^{hyp}d'_{ij}$ is shorter than the inter-receiver-station distance, the assumption that distance traveled is d_{ij} will result in a phase speed that is biased fast.

Therefore, the correct distance to be used in measuring phase speed will depend on the specific location of each source-station. The use of the composite Green's function invariably will yield a biased phase speed measurement unless the phase of the constituent source-specific interferograms are shifted prior to stacking (**section 6.2**) or if the composite Green's function is abandoned and corrections are applied to dispersion curves measured on the source-specific interferograms. Here, we report on the effect of the latter correction. To "de-bias" the phase speed measurements, we abandon the composite Green's function and measure a phase speed curve for each source-specific interferogram ($C_3(r_i, r_j; s_k)$) independently based on the more accurate ray-theoretic distance, ${}^{ell}d'_{ij}$ or ${}^{hyp}d'_{ij}$, and then average the resulting phase speed curves.

Fig. 18 presents an example of the set of source-specific phase speed curves that have been de-biased by using the source-specific ray-theoretic distances for receiver-stations M07A and M15A. Grey curves are individual Rayleigh wave phase speed measurements for individual source-specific interferograms, of which there are seven for ${}^{ell}\mathcal{I}_3^{DW}$ (**Fig. 18a**) and 26 for ${}^{hyp}\mathcal{I}_3^{DW}$ (**Fig. 18b**). Black lines and error bars indicate the mean and standard deviation (σ) of the source-specific curves. At each period we reject a source-specific measurement if it lies more than 2σ from the mean and we discard the mean measurement altogether if $\sigma > 60$ m/s, which occurs in the example of **Fig. 18** at periods greater than 40 s. **Fig. 19a** shows the mean correction applied across the entire data set for the two three-station direct-wave methods. The average standard deviation amongst the constituent source-specific curves over the entire data set is presented in **Fig. 19b**. The standard deviations for the ${}^{ell}\mathcal{I}_3^{DW}$ method are generally smaller than the ${}^{ell}\mathcal{I}_3^{DW}$ method, consistent with the latter having larger and more complex sensitivity zones (**section 5.2**). These standard deviations could serve as uncertainty estimates for the resulting dispersion measurements.

After the de-biasing correction, the mean and standard deviation of the difference between the $\mathcal{I}_3^{DW}$ and $\mathcal{I}_2^{AN}$ measurements are listed in **Table 3**, which should be contrasted with **Table 1** that contains the same statistics without the de-biasing. The correction has little effect on the standard deviation, but the mean difference between the $\mathcal{I}_3^{DW}$ and $\mathcal{I}_2^{AN}$ measurements decreases in all periods, except for ${}^{hyp}\mathcal{I}_3^{DW}$ at 80 s. If we consider the mean difference to be a measure of residual bias, then the bias of the corrected measurements is small up through 50 s period (< 7 m/s) for both three-station methods. However, it grows at longer periods for the ${}^{ell}\mathcal{I}_3^{DW}$ method up to ∼15 m/s, presumably because the ray-theoretic correction becomes less effective at longer periods. For reasons we do not fully understand, the ${}^{hyp}\mathcal{I}_3^{DW}$ method has a smaller residual bias than the ${}^{ell}\mathcal{I}_3^{DW}$ method, although the standard deviations of the differences tends to be larger. This information is presented in **Fig. 20** at all periods for comparison with **Fig. 10**.

6.2 Potential for Further Refinements

We have chosen many of the characteristics of the two-station and three-station interferometric methods in a reasoned but largely ad-hoc way. Thus, all of the procedures we describe here may be refined to improve some aspect of the results. Such refinements could be made (1) to the data processing procedures, (2) to the definition of the stationary phase zones for the direct-wave methods, (3) to the de-biasing procedure applied to the direct-wave methods, and (4) to the use of the results from the different methods in concert with one another. Finally, (5) the three-station direct-wave methods could work optimally for new generalized interferometric methods based on not estimating Green's functions.

(1) Data processing procedures include the definition of both the direct-wave and coda-wave windows, the one-wavelength criterion for the minimum inter-receiver-station distance, the chosen values of the stacking weights w_j, and the use of only of the symmetric component of the two-station ambient noise interferograms as the basis for all of data processing. In addition, the two-station data processing procedures of Shen and Ritzwoller (2016) underlie our results, including the use of an 80 s moving average time-domain normalization window and spectral whitening. All of these choices may be revised in the future to optimize the result of data processing. In particular, the stacking weights could incorporate information about the spatial distribution of source-stations (Entwistle et al., 2015). For three station coda-wave interferometry ($\mathcal{I}_3^{CW}$), performing interferometry on pre-stacked $\mathcal{I}_2$ (Zhang & Yang, 2013; Haendel et al., 2016) may greatly increase SNR because cross-talks between incoherent signals are avoided (Sheng et al., 2018). Despite its inapplicability to asynchronous pairs, this pre-stacking scheme may be promising for extraction of short-period (< 5 s) information (Sheng et al., 2018).

(2) Another important characteristic of the three-station direct-wave methods is the definition of the stationary-phase zones. We choose $\alpha = 10^{-2}$ to be period-independent,

which produces a maximum angle of both the elliptical and hyperbolic stationary phase zones of about $\theta = 8°$. An optimal period-dependent parameterization of the stationary phase zones may be possible. Moreover, because increasing α should increase the bias of the three-station methods, in station-rich settings α may be reduced and in station-poor regions it may be increased, although at the expense of increasing bias.

(3) The de-biasing method outlined in **section 6.1** applies corrections to dispersion curves before they are statistically summarized for each path, based on a great-circle ray-theoretic procedure. This method could be improved by correcting additional errors from off-great-circle propagation (e.g., Yao et al., 2006; Foster et al., 2014), non-plane waves (e.g., Pedersen, 2006) and finite-frequency effects (e.g., Yao et al., 2010; de Vos et al., 2013; Fichtner et al., 2017). Alternately, a completely different approach may be possible, which applies phase corrections to source-specific interferograms (C^3) and then makes the dispersion measurements on the composite Green's function ($\hat{G}_3$). The correction is a (frequency-dependent) phase shift to each of the source-specific interferograms prior to stacking.

(4) Because the three-station methods ($\mathcal{I}_3$) are consistent with the two-station method ($\mathcal{I}_2$), measurements from all methods can be combined simultaneously. It might be particularly advantageous to combine measurements from methods ${}^{ell}\mathcal{I}_3^{DW}$ and ${}^{hyp}\mathcal{I}_3^{DW}$ because they are oppositely biased, and their biases may cancel approximately without an explicit bias correction.

(5) New methods of interferometry are being developed that are not dependent on estimating Green's functions, but rather attempt to extract information about the propagating medium irrespective of the relative position of the sources and receiver-stations (e.g., Fichtner et al., 2017). Three-station direct-wave interferometry, where the location of source-stations is known exactly, may provide an ideal application for these methods.

7 Conclusions

Our principal finding is that the three-station direct-wave interferometry methods ${}^{ell}\mathcal{I}_3^{DW}$ and ${}^{hyp}\mathcal{I}_3^{DW}$ generally outperform three-station coda-wave interferometry $\mathcal{I}_3^{CW}$, even though direct-wave interferometry has been largely ignored as an imaging tool to date. This outperformance includes such metrics as signal-to-noise ratio, the number of measurements returned, and most notably the band-width of the measurements because $\mathcal{I}_3^{CW}$ is primarily confined to providing measurements below 25 s period. In addition, the direct-wave methods also outperform two-station interferometry in these metrics.

There are two primary caveats concerning the performance of the three-station direct-wave methods. First, the ${}^{ell}\mathcal{I}_3^{DW}$ and ${}^{hyp}\mathcal{I}_3^{DW}$ methods are slightly biased relative to two-station interferometry, $\mathcal{I}_2^{AN}$. However, we present a ray-theoretic de-biasing procedure that nearly eliminates the bias at and below about 50 s period, where ray-theory is expected to work best, and substantially reduces bias at longer periods. Second, the sensitivity kernels for the three-station direct-wave methods are more complicated than both two-station interferometry and three-station coda-wave interferometry and remain poorly understood. Research is needed to understand the nature of the sensitivity kernels for the three-station direct-wave methods and how they compare to two-station interferometry.

The results in this paper may be considered to provide proofs-of-concept based on a set of reasoned, but ad-hoc choices in developing the three-station methods. These methods may be improved by further refinements and optimization. A prominent example is how we perform the bias correction for the three-station direct-wave methods. An alternative procedure would be to phase-shift individual three-station source-specific interferograms prior to stacking, which may perform better than the de-biasing method we present here.

The tests presented here use data from the EarthScope Transportable Array (TA), but the relative merits of the various methods tested may vary in different settings where station coverage and geometries will differ. Indeed, the three-station methods that we test here may be least needed in the contiguous US due to the outstanding data coverage provided by the TA. Tests in different regions (e.g., Antarctica, Tibet, Europe, Alaska, the Juan de Fuca Plate, etc.) are needed to determine how the methods will perform in a variety of settings.

Irrespective of these caveats, we believe that three-station direct-wave interferometry promises to provide a substantial new tool to the toolbox of standard methods for imaging the structure of the crust and uppermost mantle. We encourage seismologists to bear in mind its ability to bridge asynchronously deployed stations in designing new seismic networks.

Acknowledgments

This research was supported in part by NSF grants EAR-1537868, EAR-1645269, and EAR-1928395 at the University of Colorado at Boulder. The facilities of IRIS Data Services, and specifically the IRIS Data Management Center, were used for access to waveforms, related metadata and/or derived products used in this study. IRIS Data Services are funded through the Seismological Facilities for the Advancement of Geoscience and EarthScope (SAGE) Proposal of the National Science Foundation under Cooperative Agreement EAR-1261681. This work utilized the RMACC Summit supercomputer, which is supported by the National Science Foundation (awards ACI-1532235 and ACI-1532236), the University of Colorado Boulder, and Colorado State University. The Summit supercomputer is a joint effort of the University of Colorado Boulder and Colorado State University.

References

Ansaripour, M., Rezapour, M., & Saygin, E. (2019). Shear Wave Velocity Structure of Iranian Plateau: Using Combination of Ambient Noise Cross-Correlations (C^1) and Correlation of Coda of Correlations (C^3). *Geophysical Journal International*, ggz257. doi: 10.1093/gji/ggz257

Barmin, M. P., Ritzwoller, M. H., & Levshin, A. L. (2001). A Fast and Reliable Method for Surface Wave Tomography. *Pure and Applied Geophysics*, *158*(8), 1351-1375. doi: 10.1007/978-3-0348-8264-4_3

Bensen, G. D., Ritzwoller, M. H., Barmin, M. P., Levshin, A. L., Lin, F., Moschetti, M. P., … Yang, Y. (2007). Processing seismic ambient noise data to obtain reliable broad-band surface wave dispersion measurements. *Geophysical Journal International*, *169*(3), 1239-1260. doi: 10.1111/j.1365-246X.2007.03374.x

Curtis, A., & Halliday, D. (2010). Source-receiver wave field interferometry. *Physical Review E*, *81*(4), 046601. doi: 10.1103/PhysRevE.81.046601

de Vos, D., Paulssen, H., & Fichtner, A. (2013). Finite-frequency sensitivity kernels for two-station surface wave measurements. *Geophysical Journal International*, *194*(2), 1042-1049. doi: 10.1093/gji/ggt144

Dziewonski, A., Bloch, S., & Landisman, M. (1969). A technique for the analysis of transient seismic signals. *Bulletin of the Seismological Society of America*, *59*(1), 427-444.

Entwistle, E., Curtis, A., Galetti, E., Baptie, B., & Meles, G. (2015). Constructing new seismograms from old earthquakes: Retrospective seismology at multiple length scales. *Journal of Geophysical Research: Solid Earth*, *120*(4), 2466-2490. doi: 10.1002/2014JB011607

Fenneman, N. M., & Johnson, D. W. (1946). Physical divisions of the United States. *Reston, VA: US Geological Survey.*

Fichtner, A., Stehly, L., Ermert, L., & Boehm, C. (2017). Generalised interferometry - I: Theory for inter-station correlations. *Geophysical Journal International*, *208*(2), 603-638. doi: 10.1093/gji/ggw420

Foster, A., Ekström, G., & Nettles, M. (2014). Surface wave phase velocities of the Western United States from a two-station method. *Geophysical Journal International*, *196*(2), 1189-1206. doi: 10.1093/gji/ggt454

Froment, B., Campillo, M., & Roux, P. (2011). Reconstructing the Green's function through iteration of correlations. *Comptes Rendus Geoscience*, *343*(8-9), 623-632. doi: 10.1016/j.crte.2011.03.001

Garnier, J., & Papanicolaou, G. (2009). Passive Sensor Imaging Using Cross Correlations of Noisy Signals in a Scattering Medium. *SIAM Journal on Imaging Sciences*, *2*(2), 396-437. doi: 10.1137/080723454

Haendel, A., Ohrnberger, M., & Krüger, F. (2016). Extracting near-surface QL between 1–4 Hz from higher-order noise correlations in the Euroseistest area, Greece. *Geophysical Journal International*, *207*(2), 655-666. doi: 10.1093/gji/ggw295

Halliday, D., & Curtis, A. (2009). Seismic interferometry of scattered surface waves in attenuative media. *Geophysical Journal International*, *178*(1), 419-446. doi: 10.1111/j.1365-246X.2009.04153.x

Levshin, A. L., & Ritzwoller, M. H. (2001). Automated detection, extraction, and measurement of regional surface waves. *Pure and Applied Geophysics*, *158*(8), 1531–1545. doi: 10.1007/978-3-0348-8264-4_11

Lin, F.-C., Moschetti, M. P., & Ritzwoller, M. H. (2008). Surface wave tomography of the western United States from ambient seismic noise: Rayleigh and Love wave phase velocity maps. *Geophysical Journal International*, *173*(1), 281-298. doi: 10.1111/j.1365-246X.2008.03720.x

Lin, F.-C., Ritzwoller, M. H., & Snieder, R. (2009). Eikonal tomography: Surface wave tomography by phase front tracking across a regional broad-band seismic array. *Geophysical Journal International*, *177*(3), 1091-1110. doi: 10.1111/j.1365-246X.2009.04105.x

Ma, S., & Beroza, G. C. (2012). Ambient-field Green's functions from asynchronous seismic observations. *Geophysical Research Letters*, *39*(6), L06301. doi: 10.1029/2011GL050755

Pedersen, H. A. (2006). Impacts of non-plane waves on two-station measurements of phase velocities. *Geophysical Journal International*, *165*(1), 279-287. doi: 10.1111/j.1365-246X.2006.02893.x

Ritzwoller, M. H., & Feng, L. (2019). Overview of pre- and post-processing of ambient-noise correlations. In N. Nakata, L. Gualtieri, & A. Fichtner (Eds.), *Seismic Ambient Noise.* Cambridge: Cambridge University Press. doi: 10.1017/9781108264808

Sabra, K. G., Gerstoft, P., Roux, P., Kuperman, W. A., & Fehler, M. C. (2005). Surface wave tomography from microseisms in Southern California. *Geophysical Research Letters*, *32*(14), L14311. doi: 10.1029/2005GL023155

Shapiro, N. M., & Campillo, M. (2004). Emergence of broadband Rayleigh waves from correlations of the ambient seismic noise. *Geophysical Research Letters*, *31*(7), L07614. doi: 10.1029/2004GL019491

Shapiro, N. M., Campillo, M., Stehly, L., & Ritzwoller, M. H. (2005). High-Resolution Surface-Wave Tomography from Ambient Seismic Noise. *Science*, *307*(5715), 1615-1618. doi: 10.1126/science.1108339

Shapiro, N. M., Ritzwoller, M. H., & Bensen, G. D. (2006). Source location of the 26 sec microseism from cross-correlations of ambient seismic noise. *Geophysical Research Letters*, *33*(18), L18310. doi: 10.1029/2006GL027010

Shen, W., & Ritzwoller, M. H. (2016). Crustal and uppermost mantle structure beneath the United States. *Journal of Geophysical Research: Solid Earth*, *121*(6), 4306-4342. doi: 10.1002/2016JB012887

Sheng, Y., Denolle, M. A., & Beroza, G. C. (2017). Multicomponent C3 Green's Functions for Improved Long-Period Ground-Motion Prediction. *Bulletin of the Seismological Society of America*, *107*(6), 2836-2845. doi: 10.1785/0120170053

Sheng, Y., Nakata, N., & Beroza, G. C. (2018). On the Nature of Higher-Order Ambient Seismic Field Correlations. *Journal of Geophysical Research: Solid Earth*, *123*(9), 7969-7982. doi: 10.1029/2018JB015937

Slob, E., & Wapenaar, K. (2007). Electromagnetic Green's functions retrieval by cross-correlation and cross-convolution in media with losses. *Geophysical Research Letters*, *34*(5), L05307. doi: 10.1029/2006GL029097

Snieder, R. (2004). Extracting the Green's function from the correlation of coda waves: A derivation based on stationary phase. *Physical Review E*, *69*(4), 046610. doi: 10.1103/PhysRevE.69.046610

Spica, Z., Perton, M., & Beroza, G. C. (2017). Lateral heterogeneity imaged by small-aperture *ScS* retrieval from the ambient seismic field. *Geophysical Research Letters*, *44*(16), 8276-8284. doi: 10.1002/2017GL073230

Spica, Z., Perton, M., Calò, M., Legrand, D., Córdoba-Montiel, F., & Iglesias, A. (2016). 3-D shear wave velocity model of Mexico and South US: Bridging seismic networks with ambient noise cross-correlations (C^1) and correlation of coda of correlations (C^3). *Geophysical Journal International*, *206*(3), 1795-1813. doi: 10.1093/gji/ggw240

Stehly, L., Campillo, M., Froment, B., & Weaver, R. L. (2008). Reconstructing Green's function by correlation of the coda of the correlation (C^3) of ambient seismic noise. *Journal of Geophysical Research*, *113*(B11), B11306. doi: 10.1029/2008JB005693

Yao, H., & van der Hilst, R. D. (2009). Analysis of ambient noise energy distribution and phase velocity bias in ambient noise tomography, with application to SE Tibet. *Geophysical Journal International*, *179*(2), 1113-1132. doi: 10.1111/j.1365-246X.2009.04329.x

Yao, H., van der Hilst, R. D., & de Hoop, M. V. (2006). Surface-wave array tomography in SE Tibet from ambient seismic noise and two-station analysis - I. Phase velocity maps. *Geophysical Journal International*, *166*(2), 732-744. doi: 10.1111/j.1365-246X.2006.03028.x

Yao, H., van der Hilst, R. D., & Montagner, J.-P. (2010). Heterogeneity and anisotropy of the lithosphere of SE Tibet from surface wave array tomography. *Journal of Geophysical Research: Solid Earth*, *115*(B12), B12307. doi: 10.1029/2009JB007142

Zhang, J., & Yang, X. (2013). Extracting surface wave attenuation from seismic noise using correlation of the coda of correlation. *Journal of Geophysical Research: Solid Earth*, *118*(5), 2191-2205. doi: 10.1002/jgrb.50186

Table 1. Differences (m/s) of Rayleigh wave phase speed measurements from the $\mathcal{I}_3$ methods compared to $\mathcal{I}_2$ before de-biasing correction

	$\mathcal{I}_3^{CW}$		$^{ell}\mathcal{I}_3^{DW}$		$^{hyp}\mathcal{I}_3^{DW}$	
Period (s)	Mean	SD	Mean	SD	Mean	SD
10	-0.2	3.9	-9.8	4.8	10.7	5.7
20	0.9	12.5	-11.6	6.4	13.4	8.0
30	-	-	-12.5	10.9	14.4	13.2
40	-	-	-10.9	17.5	13.2	20.7
50	-	-	-13.9	23.8	11.8	27.1
60	-	-	-17.0	28.2	9.2	31.4
70	-	-	-18.7	30.2	5.1	34.5
80	-	-	-17.2	31.1	1.2	36.5

Table 2. Differences (m/s) of Rayleigh wave phase speed maps from the $\mathcal{I}_3$ methods compared to $\mathcal{I}_2$

	$\mathcal{I}_3^{CW}$		$^{ell}\mathcal{I}_3^{DW}$		$^{hyp}\mathcal{I}_3^{DW}$	
Period (s)	Mean	SD	Mean	SD	Mean	SD
10	0.7	4.6	-8.4	4.3	7.5	4.3
20	-0.6	7.6	-12.5	4.0	9.9	3.9
30	-	-	-20.6	6.1	7.8	6.2
40	-	-	-29.3	11.3	3.1	10.2
50	-	-	-33.9	17.6	0.1	16.5
60	-	-	-39.8	25.0	-5.0	22.2

Table 3. Differences (m/s) of Rayleigh wave phase speed measurements from the direct-wave $\mathcal{I}_3$ methods compared to $\mathcal{I}_2$ after de-biasing correction

	${}^{ell}\mathcal{I}_3^{DW}$		${}^{hyp}\mathcal{I}_3^{DW}$	
Period (s)	Mean	SD	Mean	SD
10	-0.0	5.5	0.1	7.8
20	1.1	7.2	0.0	9.3
30	0.5	11.5	-1.1	15.3
40	-2.3	17.7	1.8	23.7
50	-6.5	24.2	6.0	29.3
60	-10.0	28.0	7.0	31.6
70	-13.3	28.4	4.8	32.6
80	-15.1	27.4	1.9	33.0

Figures:

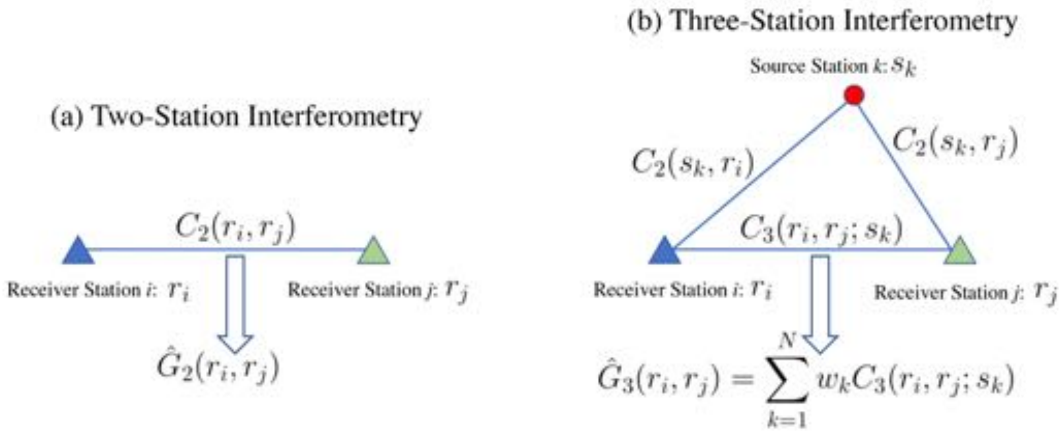

Figure 1. Notation for interferometry. (a) Two-station interferometry. $C_2(r_i, r_j)$ is the cross-correlation between processed seismograms recorded at receiver-stations r_i and r_j. The two-station estimated Green's function, $\hat{G}_2(r_i, r_j)$, can be determined from C_2 after applying an appropriate phase shift. Receiver-stations r_i and r_j must operate synchronously. (b) Three-station interferometry. Cross-correlations between seismograms recorded at each source-station, s_k, with records at receiver-stations, r_i and r_j, are denoted $C_2(s_k, r_i)$ and $C_2(s_k, r_j)$. Direct-wave or coda-wave parts of these records are cross-correlated or convolved to measure the source-specific interferogram, $C_3(r_i, r_j; s_k)$, which can be summed over contributions from many source-stations to produce the three-station composite Green's function, $\hat{G}_3(r_i, r_j)$, between the receiver-stations. Receiver-stations r_i and r_j need not operate synchronously with one another, but both must overlap the operation of each source-station.

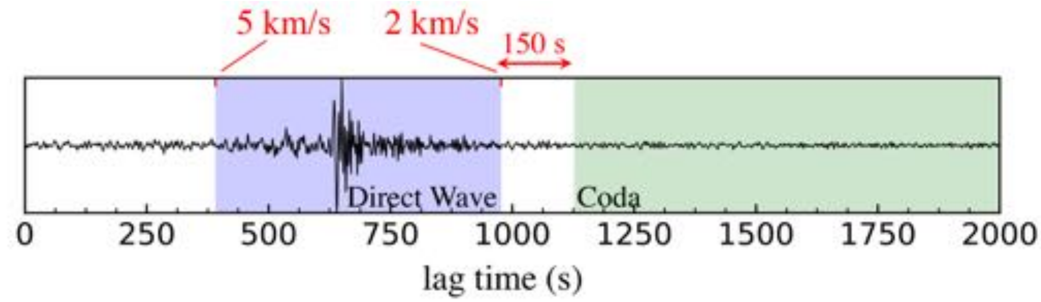

Figure 2. Example of the definition of the direct-wave and coda-wave segments of a two-station cross-correlation of ambient noise, C_2, for stations ANMO (Albuquerque, NM) and M47A (Cromwell, NM), at an inter-station distance of ∼1950 km. The direct-wave is the segment of the record between times corresponding to group speeds of 2 and 5 km/s. The coda-wave segment starts 150 s after the end of the direct-wave, and extends to the end of 3000 s. The symmetric component of the cross-correlation is shown (average of positive and negative correlation lags).

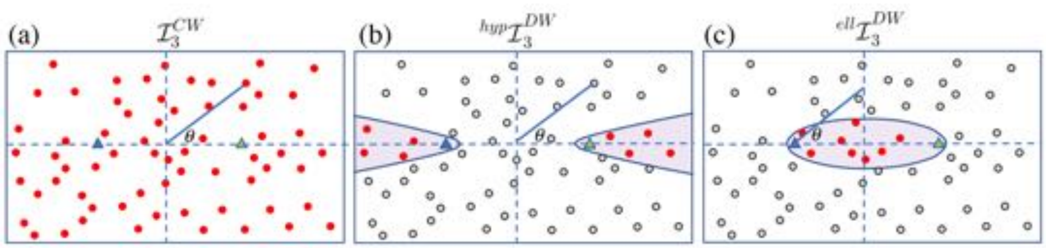

Figure 3. Schematic illustration of the geometrical constraints on source-stations for different methods of three-station interferometry. The two receiver-stations are shown with the bue and green triangles, and the circles are locations of other stations that may act as source-stations. Those stations that can act as source-stations are shown with red circles and those cannot with grey circles. (a) For three-station coda-wave interferometry, $\mathcal{I}_3^{CW}$, all stations whose operation overlaps the two receiver-stations can act as a source-station. (b) For three-station direct-wave interferometry with source-stations radially outside the receiver-stations, ${}^{hyp}\mathcal{I}_3^{DW}$, source-stations must lie in stationary phase hyperbolae (purple shading). (c) For three-station direct-wave interferometry with source-stations between the receiver-stations, ${}^{ell}\mathcal{I}_3^{DW}$, source-stations must lie in the stationary phase ellipse (purple shading). The angle θ in each case is defined in **section 3** and used in **Fig. 5**.

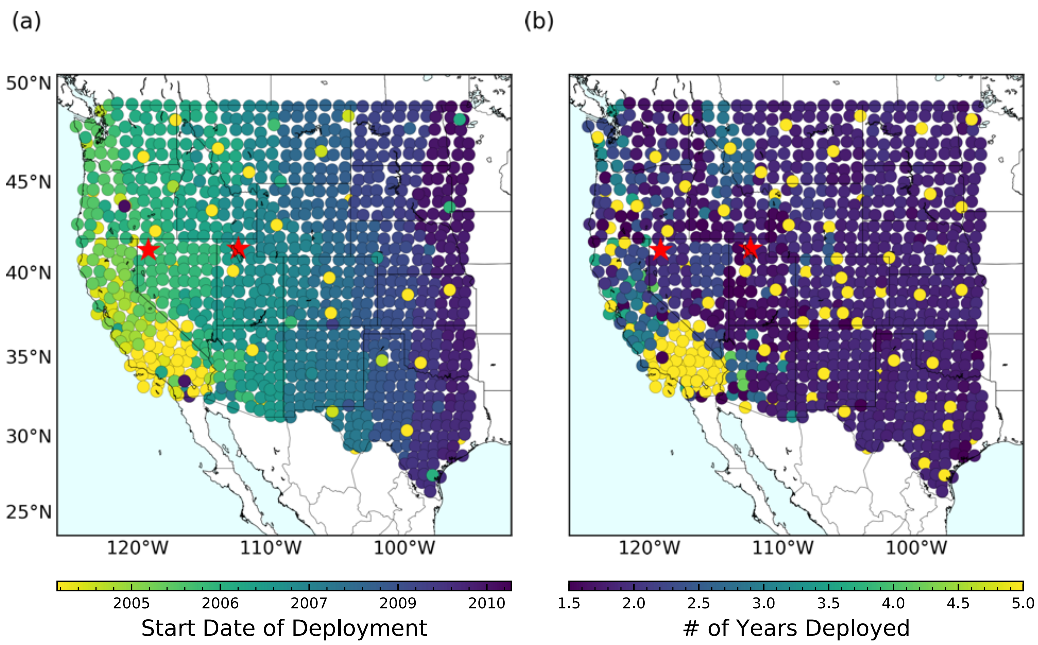

Figure 4. Map of stations used in this study. Red stars mark stations used in **Figs 5 - 7** and **18**: M07A (Soldier Meadow, NV) and M15A (Promontory, UT). (a) The start dates for each station are color-coded, showing a rolling pattern from west to east. (b) Duration of deployment is color-coded. Most stations are deployed around two years with a few much longer from the USArray Reference Network (_US-REF) and the Southern California Seismic Network (CI).

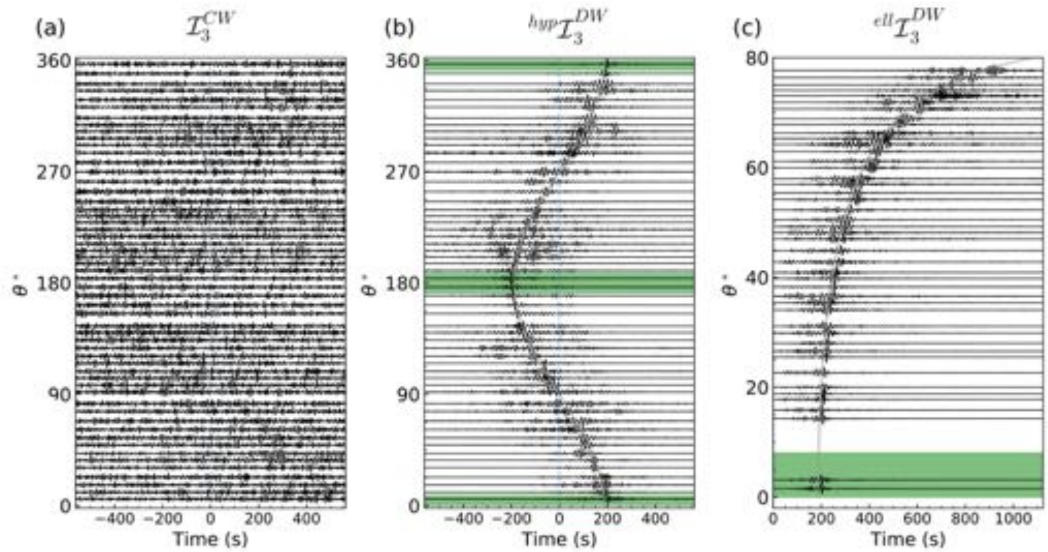

Figure 5. Example record sections of three-station interferograms for the receiver-station pair M07A-M15A, whose locations are shown in **Fig. 4** . (a) Coda-wave interferograms (C_3^{CW}) for different source-stations plotted at the azimuth angle θ shown in **Fig. 3a**. (b) Direct-wave interferograms (C_3^{DW}) plotted for source-stations at the azimuth angle shown in **Fig. 3b**. The green regions are the hyperbolic stationary-phase zones for ${}^{hyp}\mathcal{I}_3^{DW}$. (c) Direct-wave interferograms (C_3^{DW}) plotted for source-stations at the azimuth angle shown in **Fig. 3c**. Only positive time lags are defined. The green region is the elliptical stationary-phase zone for ${}^{ell}\mathcal{I}_3^{DW}$. Grey curves in (b) and (c) are predictions from eqs. (4) and (5), respectively, with $c = 3$ km/s. Only selected three-station interferograms are shown to ease visualization.

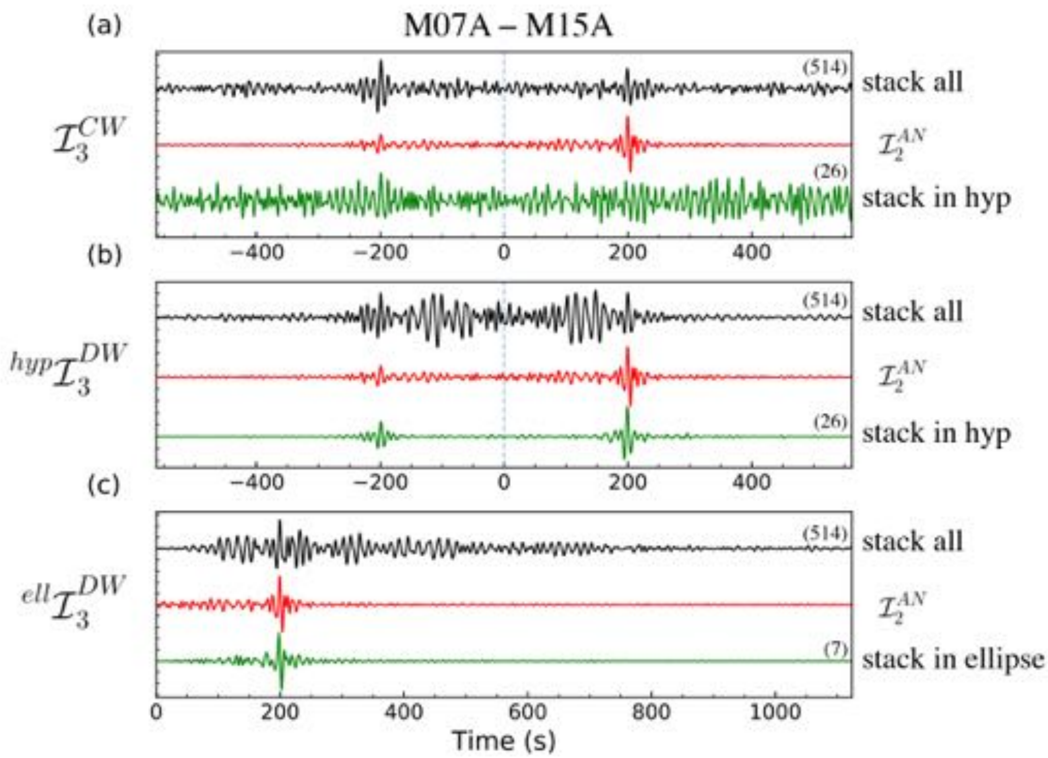

Figure 6. Examples of stacks of three-station interferograms for the receiver-station pair M07A-M15A of **Fig. 5**. In each panel the two-station estimated Green's function ($\mathcal{I}_2^{AN}$) is plotted for reference (red). The number of source-stations for each stack is shown in parentheses above the stacked trace. (a) Method $\mathcal{I}_3^{CW}$. Two stacks of coda-wave interferograms are shown: (black line, stack all) stack of the interferograms from all source-stations irrespective of the azimuthal angle θ (defined in **Fig. 3a**) and (green line, stack hyp) stack of the coda-wave interferograms for sources in the hyperbolic stationary phase zone. For $\mathcal{I}_3^{CW}$, the black line is the composite Green's function. (b) Method ${}^{hyp}\mathcal{I}_3^{DW}$. Black and green lines have similar meanings to those in (a), but here the direct-wave interferograms are stacked. For ${}^{hyp}\mathcal{I}_3^{DW}$, the green line is the composite Green's function. (c) Method ${}^{ell}\mathcal{I}_3^{DW}$. Black line is the same as in (b), but the green line is the stack of direct-wave interferograms in the elliptical stationary phase zone. For ${}^{ell}\mathcal{I}_3^{DW}$, the green line is the composite Green's function and only positive time lags are defined.

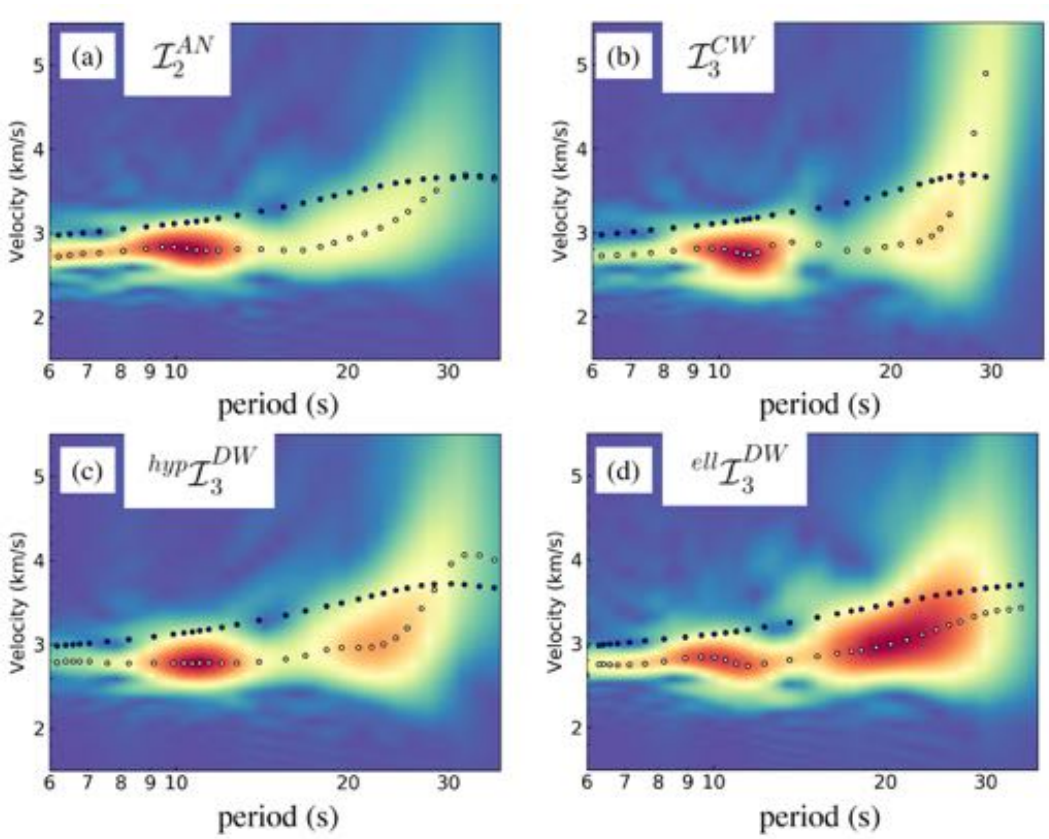

Figure 7. Frequency-time analysis (FTAN) diagrams for the receiver pair M07A-M15A using the waveforms from **Fig. 6**: (a) $\mathcal{I}_2^{AN}$, (b) $\mathcal{I}_3^{CW}$, (c) ${}^{hyp}\mathcal{I}_3^{DW}$, and (d) ${}^{ell}\mathcal{I}_3^{DW}$. White and blue circles are group and phase speed measurements, respectively.

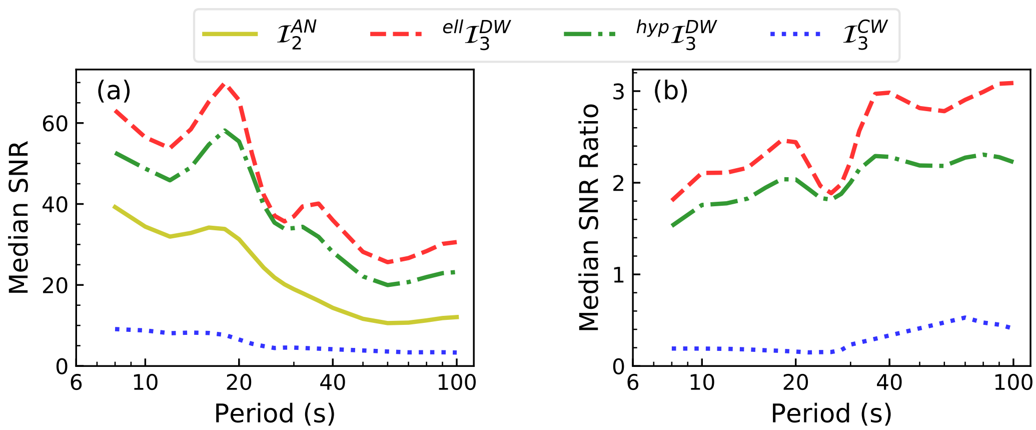

Figure 8. Signal-to-noise ratio (SNR) of estimated Green's functions for the different interferometric methods (see legend) plotted versus period. (a) Median of the SNR for each method taken over all measurements at each period. SNR generally decreases with period for all methods, but the highest SNR is from the three-station direct-wave method with an elliptical stationary phase zone ($^{ell}\mathcal{I}_3^{DW}$) and the lowest is from the three-station coda-wave method ($\mathcal{I}_3^{CW}$). (b) Paths common to two-station and three-station interferometry in (a) are selected such that the ratio of the median SNR for each three-station method to that for the two-station method is shown. The direct-wave methods increase SNR relative to $\mathcal{I}_2^{AN}$ by a factor ranging from about 1.5 to 3 which grows with period, whereas the coda-wave method reduces SNR by a factor of 3-5.

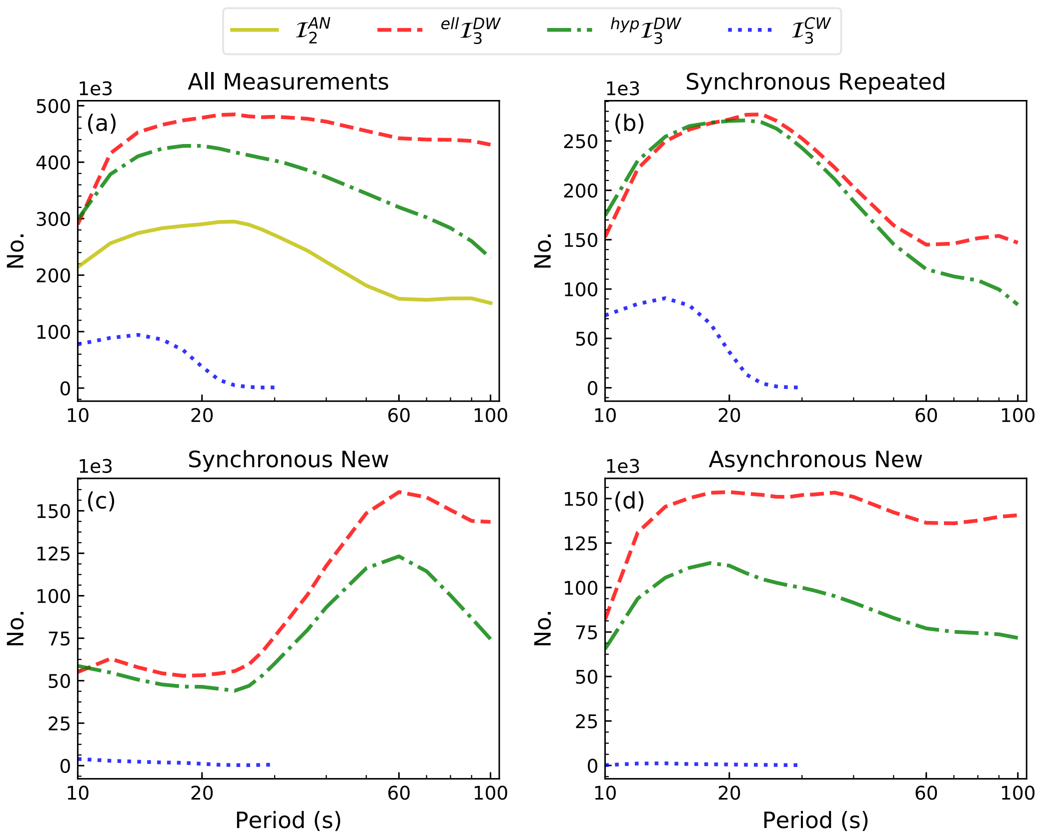

Figure 9. Number of measurements versus period. (a) Number of accepted Rayleigh wave phase speed measurements plotted versus period for the different interferometric methods (see legend). The largest nunber of measurements is from the three-station direct-wave method with an elliptical stationary phase zone ($^{ell}\mathcal{I}_3^{DW}$) and the smallst number is from the three-station coda-wave method ($\mathcal{I}_3^{CW}$). The total number of measurements can be broken into three parts, as shown in (b)-(d). (b) Number of synchronous measurements from three-station interferometry methods ($\mathcal{I}_3$) that are non-existent for two-station interferometry $\mathcal{I}_2^{AN}$ (because of low SNR). (c) Number of asynchronous measurements from $\mathcal{I}_3$ that are non-existent for $\mathcal{I}_2^{AN}$ (because of asynchrony). (d) Number of measurements from $\mathcal{I}_3$ that are redundant for $\mathcal{I}_2^{AN}$.

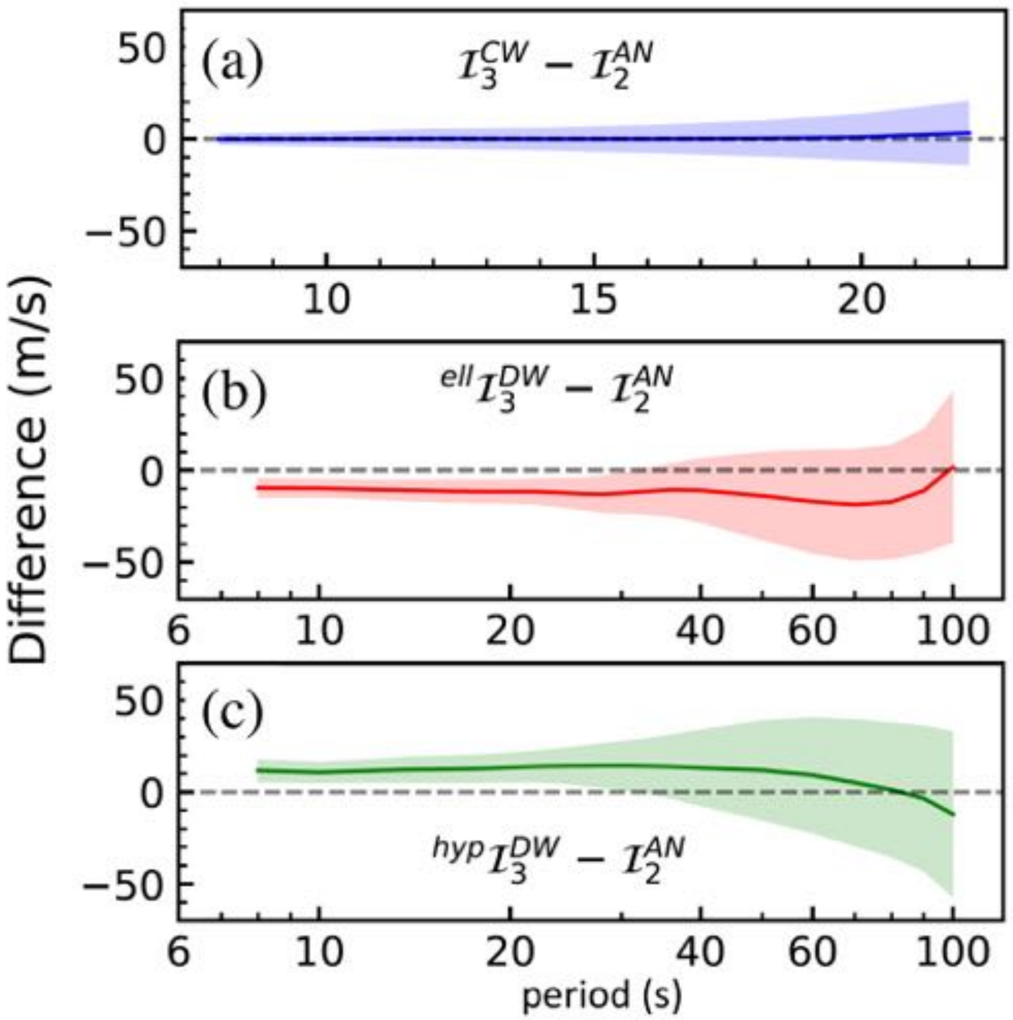

Figure 10. Fig. depicting the mean and standard deviation of the difference between Rayleigh wave phase speed measurements from the three-station methods ($\mathcal{I}_3$) and the two-station ($\mathcal{I}_2^{AN}$) method. No bias correction has been applied. Measurements from the direct-wave three-station methods ($\mathcal{I}_3^{DW}$) are systematically shifted from the $\mathcal{I}_2^{AN}$ measurements, albeit with different signs, whereas the coda-wave measurements ($\mathcal{I}_3^{CW}$) are not shifted relative to those from $\mathcal{I}_2^{AN}$. The standard deviation of the differences between the three-station and two-station measurements grow with period.

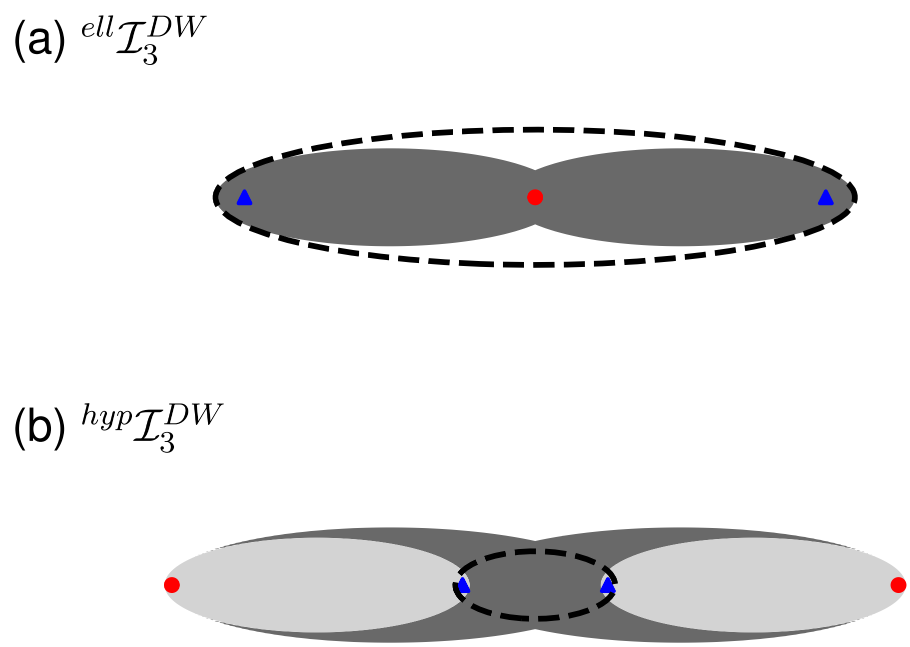

Figure 11. Schematic illustration contrasting the sensitivity kernels for ${}^{ell}\mathcal{I}_3^{DW}$ and ${}^{hyp}\mathcal{I}_3^{DW}$ with that for $\mathcal{I}_2$ which is shown as a Fresnel ellipse encompassing the two receiver-stations (blue triangles) and is depicted with the dashed lines. (a) The sensitivity kernel for ${}^{ell}\mathcal{I}_3^{DW}$ is a superposition of the two elliptical Fresnel zones where the source-station (red dot) is at one focus and each of the receiver-stations are at the other foci. The resulting sensitivity kernel for ${}^{ell}\mathcal{I}_3^{DW}$ (grey region) is smaller than the kernel for $\mathcal{I}_2$ (zone encompassed by the dashed line). (b) The sensitivity kernel for ${}^{hyp}\mathcal{I}_3^{DW}$ is the difference of the two elliptical Fresnel zones where each source-station (red dots) is at one focus and each of the receiver-stations is at the other focus. The resulting sensitivity kernel for ${}^{hyp}\mathcal{I}_3^{DW}$ (grey region) is more complicated and larger than the kernel for $\mathcal{I}_2$ (zone encompassed by the dashed line).

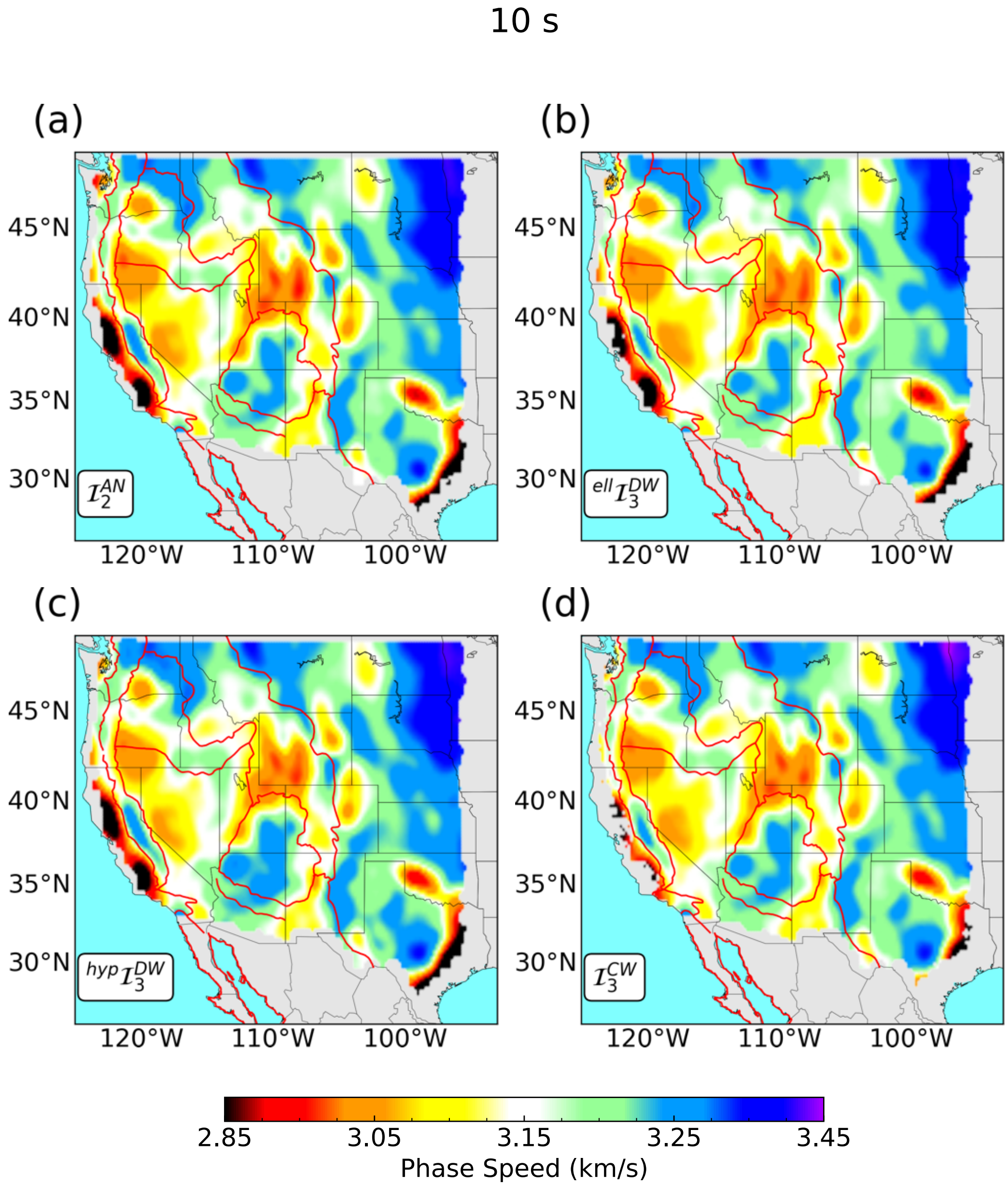

Figure 12. Rayleigh wave phase speed maps constructed with eikonal tomography at 10 s period using four different interferometric methods: (a) traditional two-station ambient noise interferometry ($\mathcal{I}_2^{AN}$), (b) three-station direct-wave interferometry with elliptical stationary phase zone ($^{ell}\mathcal{I}_3^{DW}$), (c) three-station direct-wave interferometry with hyperbolic stationary phase zone ($^{hyp}\mathcal{I}_3^{DW}$), and (d) three-station coda-wave interferometry ($\mathcal{I}_3^{CW}$). Red lines depict geological provinces (Fenneman & Johnson, 1946).

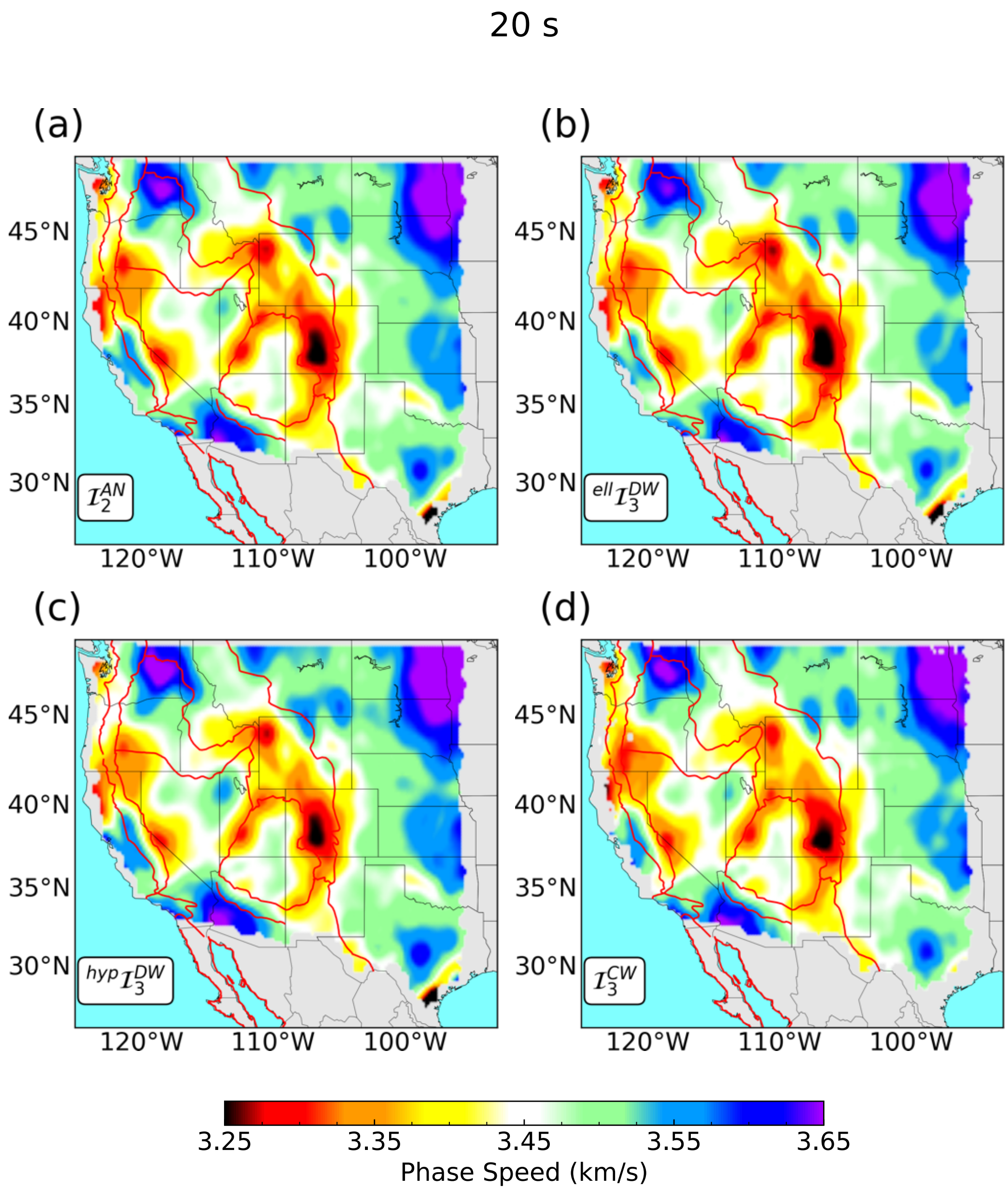

Figure 13. Similar to Fig. 12, but at 20 s period.

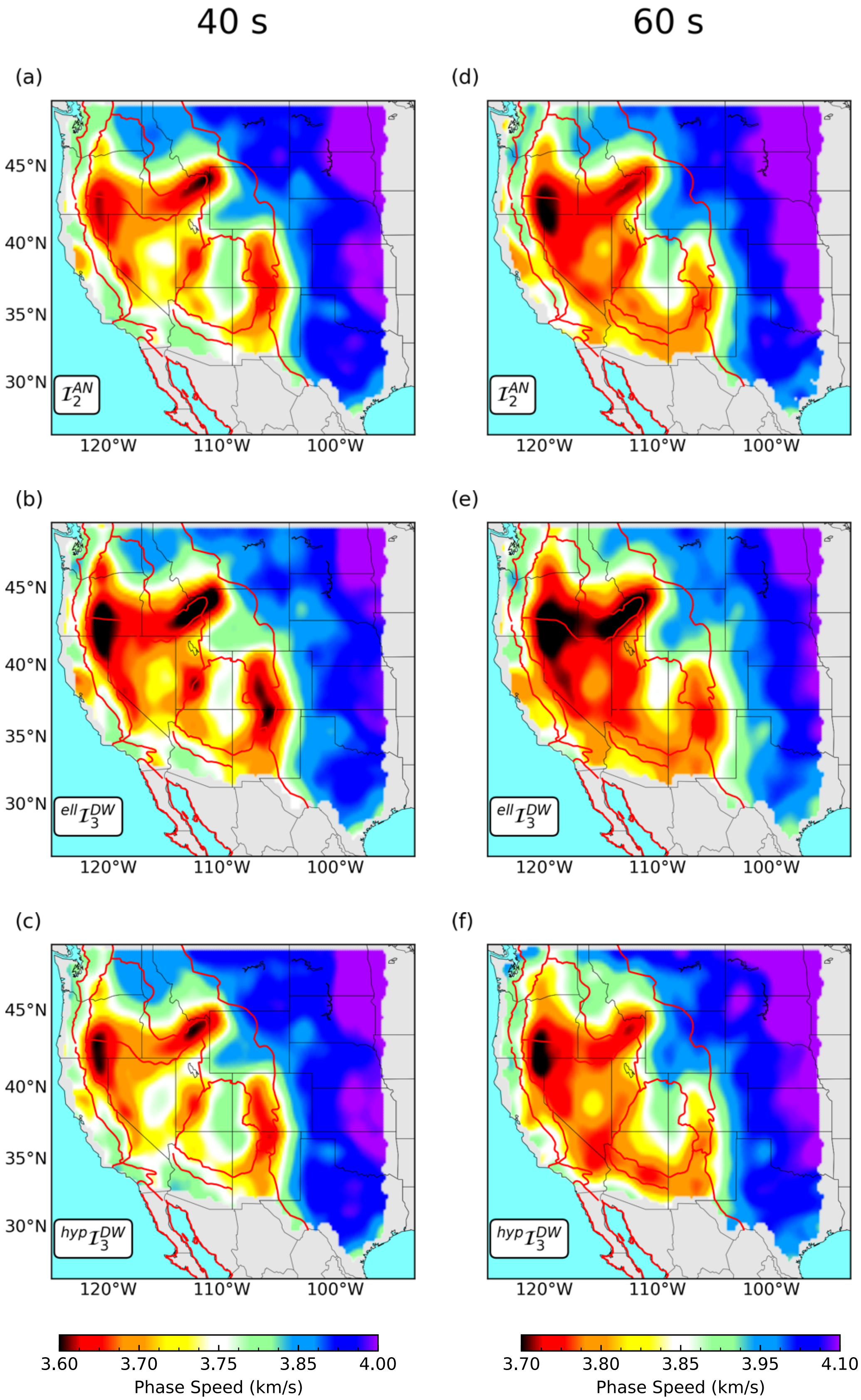

Figure 14. Similar to Fig. 12, but at periods of 40 and 60 s. $\mathcal{I}_3^{CW}$ yielded too few measurements to produce a tomographic map at these periods.

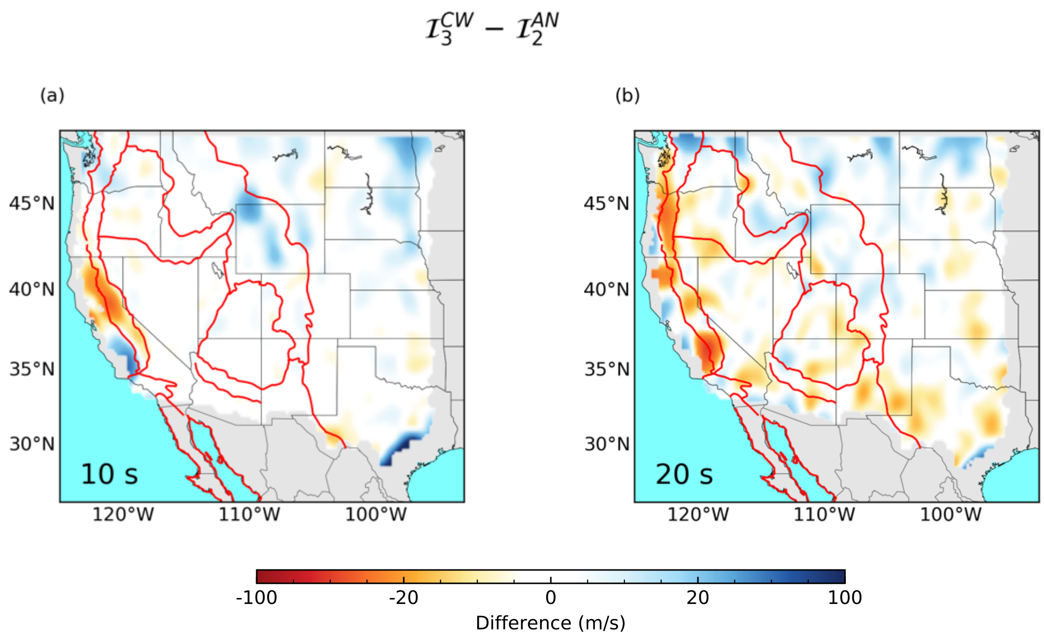

Figure 15. Differences in Rayleigh wave phase speed maps (**Figs 12** and **13**) between three-station coda-wave interferometry ($\mathcal{I}_3^{CW}$) and two-station ambient noise interferometry ($\mathcal{I}_2^{AN}$). $\mathcal{I}_3^{CW}$ yields too few measurements to produce tomographic maps at longer periods.

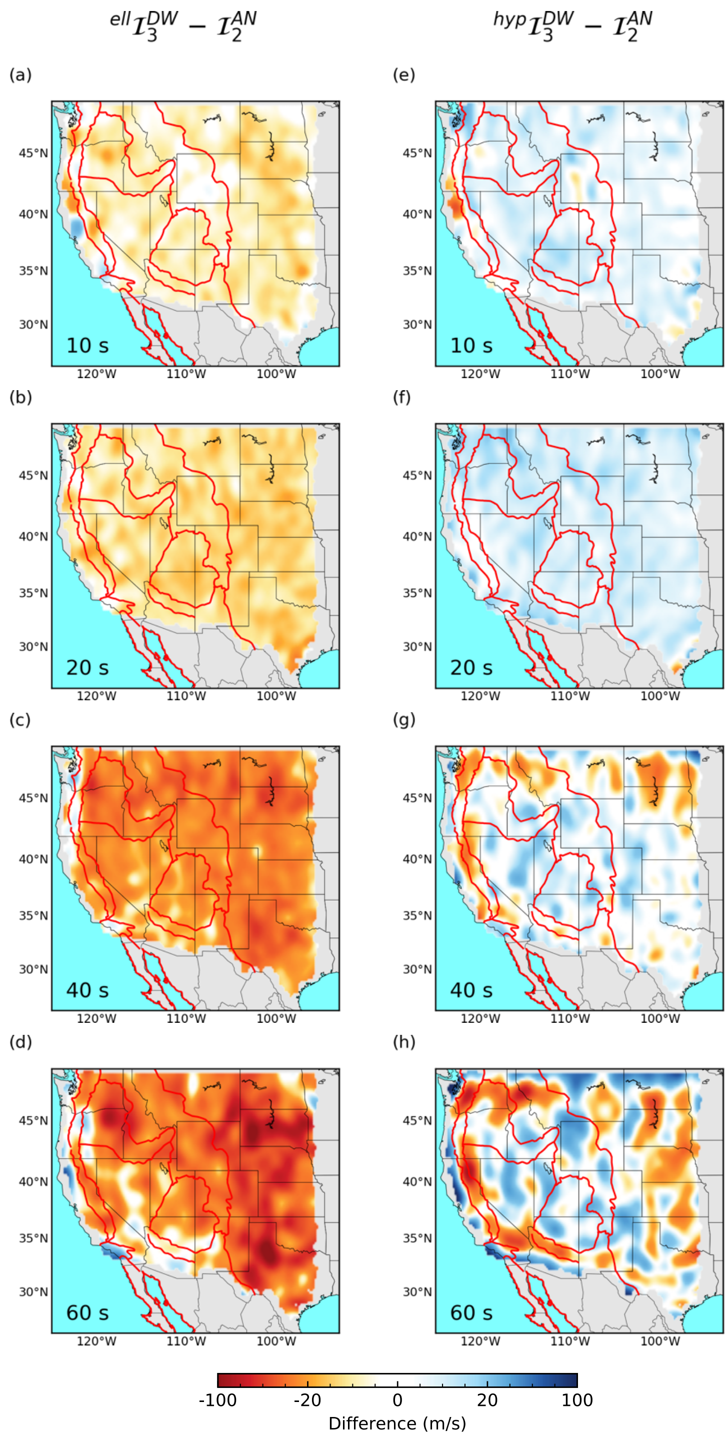

Figure 16. Similar to **Fig. 15** except differences are between three-station direct-wave interferometry and $\mathcal{I}_2^{AN}$ (**Figs 12 - 14**), and results are presented at four periods: 10 s, 20 s, 40 s, and 60 s. (a)-(d) The $^{ell}\mathcal{I}_3^{DW}$ maps are systematically slower relative to the $\mathcal{I}_2^{AN}$ maps and the standard deviation of the difference increases with period. (e)-(h) The $^{hyp}\mathcal{I}_3^{DW}$ maps are systematically faster relative to the $\mathcal{I}_2^{AN}$ maps and the standard deviation of the difference increases with period.

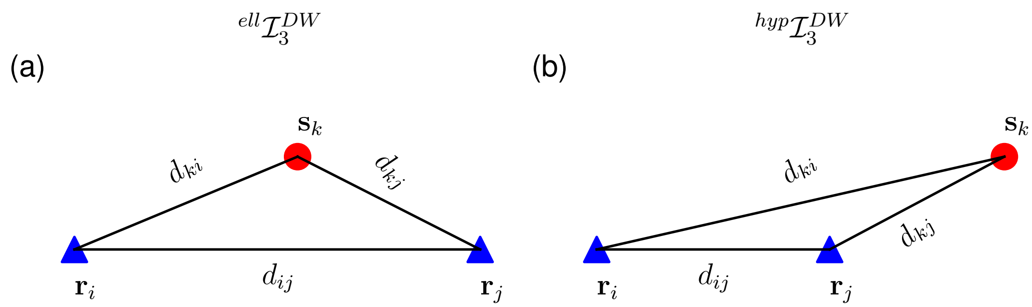

Figure 17. Geometry of the source-station (s_k) and receiver-stations (r_i, r_j) used to determine the bias correction for the three-station direct-wave methods: (a) $^{ell}\mathcal{I}_3^{DW}$ and (b) $^{hyp}\mathcal{I}_3^{DW}$.

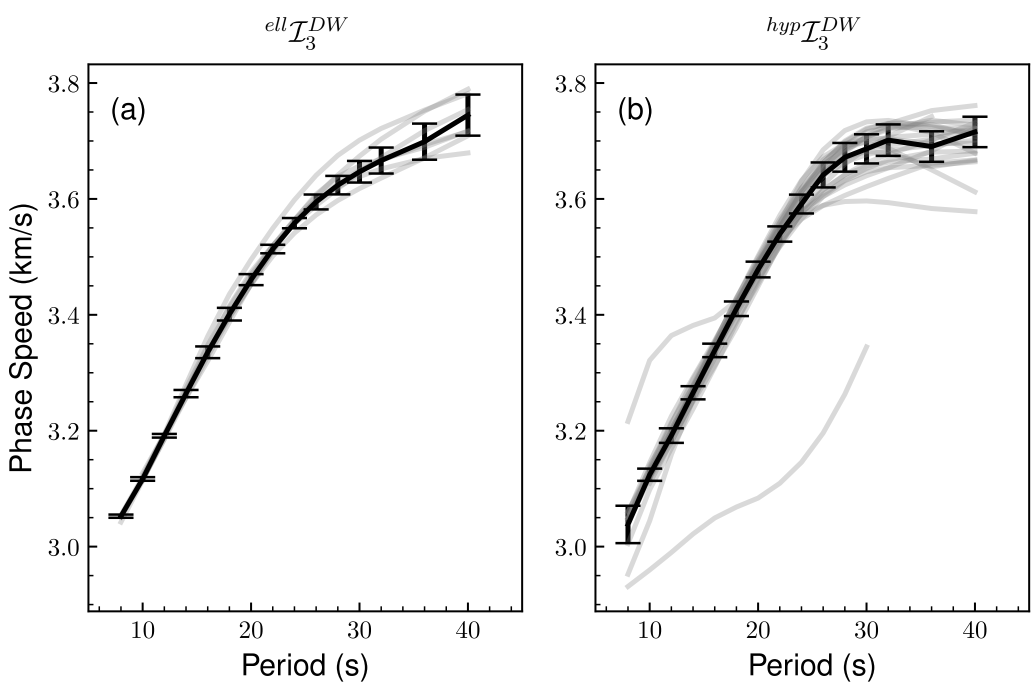

Figure 18. Examples of the de-biased Rayleigh wave phase speed curves for the receiver-station pair M07A-M15A for the two three-station direct-wave methods: (a) $^{ell}\mathcal{I}_3^{DW}$ and (b) $^{hyp}\mathcal{I}_3^{DW}$. Each gray curve is measured on a single source-specific interferogram, where there are 7 source-stations for $^{ell}\mathcal{I}_3^{DW}$ and 26 source-stations for $^{ell}\mathcal{I}_3^{DW}$. The mean and standard deviation of the constituent curves are plotted with the black line and error bars, respectively.

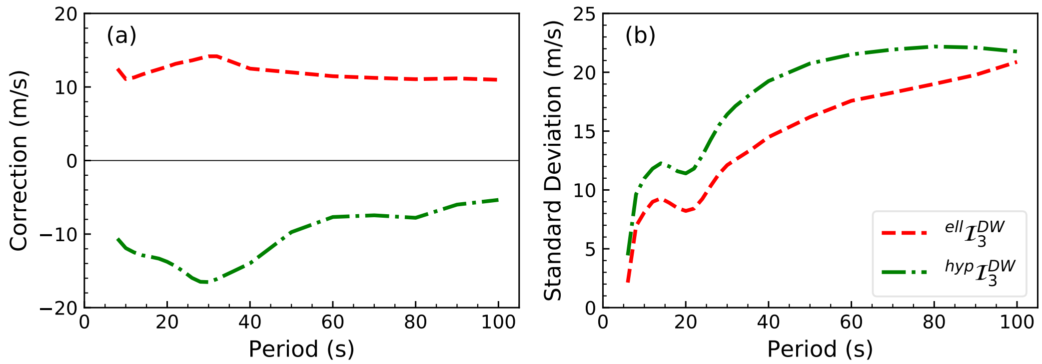

Figure 19. (a) Mean de-biasing correction averaged over all receiver-station pairs in the data set for $^{ell}\mathcal{I}_3^{DW}$ (red line) and $^{hyp}\mathcal{I}_3^{DW}$ (green line). (b) Standard deviation of the de-biased dispersion curves averaged over all receiver-station pairs in the data set.

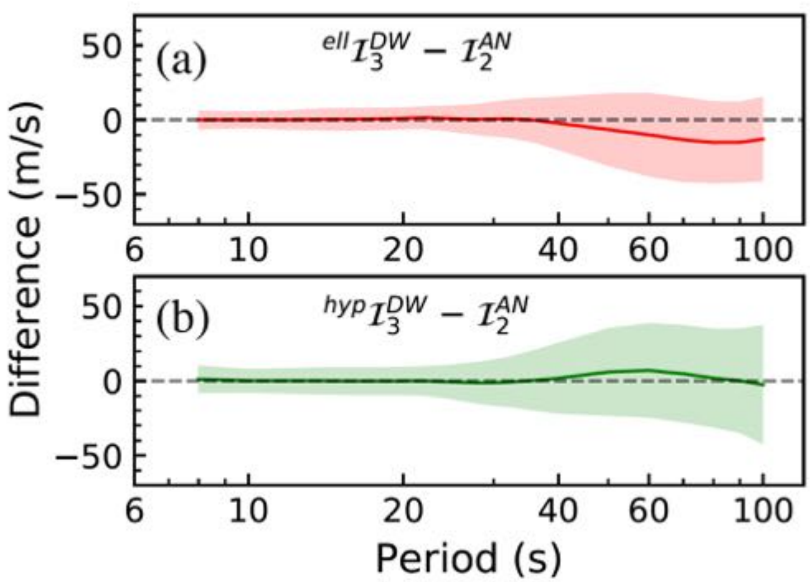

Figure 20. Similar to **Fig. 10**, but the three-station direct-wave methods ($\mathcal{I}_3^{DW}$) have been de-biased based on ray-theory. Systematic differences in Rayleigh wave phase speed measurements compared to the $\mathcal{I}_2^{AN}$ method are largely removed at periods below 40 s, and are reduced at all periods below 80 s compared to the uncorrected values. The standard deviation of the differences between the three-station and two-station measurements are not appreciably affected by the de-biasing correction.